Permeability Modeling and Electric-Hydraulic Analogy for Unidirectional Tows

by

Güldane Damla Pınarlık

A Dissertation Submitted to the
Graduate School of Sciences and Engineering
in Partial Fulfillment of the Requirements for
the Degree of

Master of Science

in

Mechanical Engineering

KOÇ ÜNİVERSİTESİ

December, 2024

Permeability Modeling and Electric-Hydraulic Analogy for Unidirectional Tows

Koç University

Graduate School of Sciences and Engineering

This is to certify that I have examined this copy of a master's thesis by

Güldane Damla Pınarlık

and have found that it is complete and satisfactory in all respects,

and that any and all revisions required by the final

examining committee have been made.

Committee Members:

____

Prof. Dr. E. Murat Sözer (Advisor)

____

Asst. Prof. Barış Çağlar

____

Prof. Dr. Metin Muradoğlu

Date: ______________________

ABSTRACT

Permeability Modeling and Electric-Hydraulic Analogy for Unidirectional Tows

Güldane Damla Pınarlık

Master of Science in Mechanical Engineering

December, 2024

This study investigates the permeability of fiber tow domains using ANSYS Fluent simulations and an approximation method based on an electric-hydraulic analogy derived from Darcy's Law and Ohm's Law. The permeability of a hexagonally distributed fiber structure is calculated using a representative unit cell modeled in ANSYS Fluent. Fibers are modeled as solid regions, allowing resin to flow through the spaces between them. Permeability is determined by applying Darcy's Law to the computed flow rate, showing strong agreement with Gebart's analytical solution. In a larger scale, the overall permeability is determined by simulating resin flow through a unit cell of ten fiber tows, where tows are treated as porous regions with resin flowing through both inter-tow and intra-tow channels. A variety of tow distribution scenarios are examined, including manually designed extreme cases and random distributions generated in MATLAB, emphasizing the impact of tow spacing perpendicular to the flow direction on flow channels and permeability. The permeability approximation method aligns with simulation results, while significantly reducing computational cost and time. Key factors such as domain size, tow spacing, and intra-tow porosity are analyzed. Comparisons between simulated and approximated permeabilities highlight the limitations of the method under varying domain sizes and intra-tow porosities. The results show that the approximation improves in accuracy as intra-tow porosity decreases and domain height increases, due to the predominance of resin flow in inter-tow channels. This study's primary contribution is offering a scalable and efficient permeability prediction approach applicable to a range of tow configurations, providing valuable insights for optimizing resin flow in composite manufacturing processes.

ÖZETÇE

Kompozit Fiber Demetlerinde Geçirgenliğin Modellemesi ve Elektrik-Hidrolik Analoji ile Hesaplanması

Güldane Damla Pınarlık

Makine Mühendisliği, Yüksek Lisans

Aralık 2024

Bu çalışma, kompozit fiber demetlerinde geçirgenlik değerini ANSYS Fluent simülasyonları ve Darcy Kanunu ile Ohm Kanunu'ndan türetilen bir elektrik-hidrolik analoji yöntemi kullanarak incelemektedir. Altıgen dağılıma sahip fiberlerin geçirgenliği, ANSYS Fluent'te modellenen temsili bir birim hücre aracılığıyla hesaplanmıştır. Simülasyonda fiberler katı bölge olarak modellenerek reçinenin fiberler arasından akışına izin verilmiştir. Geçirgenlik değeri, Darcy Kanunu'nu kullanarak simülasyondan elde edilen akış hızı üzerinden hesaplanmış ve analitik Gebart çözümüyle karşılaştırıldığında uyumlu sonuçlar verdiği görülmüştür. Daha büyük ölçekte, kompozit malzeme geçirgenliği, on fiber demetinden oluşan bir birim hücredeki reçine akış simülasyonu ile hesaplanmıştır. Buradaki demetler gözenekli bölgeler olarak tanımlanmış ve demet içinde ve dışındaki reçine akışına izin veirlmiştir. Çeşitli demet dağılım senaryoları incelenmiştir. Senaryolar arasında manuel olarak tasarlanmış ekstrem durumlar ve MATLAB ile oluşturulan rastgele dağılımlar kullanılmıştır. Bu senaryolar, akış yönüne dik demetler arası boşluğun, akış kanalları ve geçirgenlik üzerindeki etkilerini incelemek için tasarlanmıştır. Elektrik-hidrolik analoji ile yapılan geçirgenlik tahmini, simülasyon sonuçlarıyla uyum göstermiştir. Bu yöntem, bilgisayar hesaplama süresi ve maliyetini büyük ölçüde azaltmaktadır. Model alanı boyutu, demetler arası boşluk ve demet içi gözeneklilik gibi faktörler analiz edilmiştir. Simülasyon ve tahmini sonuçlar karşılaştırıldığında, model boyutlarının ve demet içi gözeneklilik değerlerinin tahmini sonuçları etkilediği gözlemlenmiştir. Sonuçlar, demet içi gözeneklilik azaldıkça ve alan yüksekliği arttıkça, tahmin yönteminin doğruluğunun arttığını göstermektedir. Bu durum, reçinenin büyük ölçüde demetler arası kanallardan akmasından kaynaklanmaktadır. Bu çalışmanın en büyük katkısı, farklı fiber demeti dağılımlarına uygulanabilmesi, ölçeklendirilebilir olması ve verimli bir geçirgenlik tahmin yöntemi sunmasıdır. Bu sayede, kompozit üretim süreçlerinde reçine akış davranışının optimize edilmesine katkı sağlamaktadır.

AKNOWLEDGEMENTS

I would like to express my deepest gratitude to my thesis advisor Prof. Dr. Murat Sözer for his guidance, expertise, and unwavering support throughout the research. His insightful feedback and encouragement have been crucial to the successful completion of this work.

I would like to thank Asst. Prof. Barış Çağlar for his constructive comments and valuable insights, which has great contribution to this project.

I am also thankful to thesis committee member Prof. Dr. Metin Muradoğlu for his thoughtful evaluations.

Special thanks to Ali Bora Albayraktar for his support and collaboration. His assistance is greatly appreciated and contributed significantly to the success of this project.

Lastly, I wish to extend my heartfelt appreciation to my family and friends for their emotional support and encouragement through this period. Their unwavering belief in me and their constant support provided the strength and motivation needed to complete this project.

TABLE OF CONTENTS

LIST OF TABLES

LIST OF FIGURES

ABBREVIATIONS

Symbol	Parameter	Unit
A	Cross-sectional area	m^2
I	Electric current	A
K	Permeability	m^2
K_t	Intra-tow permeability	m^2
K_o	Overall permeability	m^2
$K_{o,sim}$	Simulated overall permeability	m^2
$K_{o,app}$	Approximated overall permeability	m^2
L	Domain length	m
P	Liquid (resin) pressure	Pa
Q	Volumetric flowrate	m^3/s
R	Electric resistance	Ω
S	Source term	kg/m^2s^2
V	Voltage	V
V_f	Fiber volume fraction	unitless
H	Domain height	m
Z	Domain thickness	m
c	Major axis of tows	m
d	Minor axis of tows	m
e	x-distance (space) between adjacent tow centers	m
f	y-distance (space) between adjacent tow centers	m
g	Gravitational acceleration	m/s^2
h	Channel gap (space between adjacent tows)	m
$\dot{m}$	Mass flow rate	kg/s
r	Fiber radius	m
t	Time	s
u	Liquid (resin) velocity	m/s
μ	Viscosity	$Pa.s$
ρ	Density	kg/m^3
ϕ_s	Inter-tow porosity	unitless
ϕ_t	Intra-tow porosity	unitless
ϕ_o	Overall porosity	unitless

Chapter 1:
INTRODUCTION

1.1 *Properties of Composite Materials*

Composites are formed by combining two or more materials with different physical or chemical properties to create a material with enhanced characteristics. The individual components within the composite remain distinct, preserving their unique properties rather than dissolving into a single phase. Together in composite form, they exhibit improved qualities [1].

A composite typically consists of a matrix and reinforcing material. The reinforcement provides high strength and stiffness, carrying the structural load and reducing thermal stresses [1]. Meanwhile, the matrix holds the reinforcement in place, protecting it from external factors such as elevated temperatures, high humidity, or UV light. When a composite is subjected to external forces, the matrix distributes the load evenly across the reinforcement to prevent damage [1].

Fiber reinforced polymer-matrix composites are widely used in industries such as aerospace, automotive and marine due to their lightweight nature and desirable mechanical properties, including high specific strength, stiffness, toughness, and durability under harsh environmental conditions.

However, variations in raw material (e.g., fiber reinforcement) and mold preparation labor can lead to manufacturing defects resulting in part rejection. To manufacture composite parts in a cost-efficient way, optimization of the manufacturing process, including materials, mold and process parameters, through mathematical modeling and computational solutions is helpful for design engineers.

1.2 *Permeability and Darcy's Law*

Predicting the permeability of a porous fiber reinforcement is critical, as it is an important material parameter. Permeability defines how easily resin can flow through a porous medium composed of dry fiber bundles [1]. It can be defined by an empirical formula used in composite modelling, known as Darcy's Law. Darcy's Law presents a relationship between resin flow rate and the pressure gradient. Darcy's Law is expressed as in Equation (1.1), where Q is the volumetric flow rate of resin, K is permeability, A is the cross-sectional area, μ is viscosity and $\frac{\partial p}{\partial x}$ is the pressure gradient [2].

$$Q = -\frac{KA}{\mu}\frac{\partial p}{\partial x} \tag{1.1}$$

In liquid composite molding processes, permeability plays a pivotal role in controlling resin flow, ensuring uniform resin distribution and minimizing defects like voids and dry spots. Permeability is influenced by a combination of material, structural, fluid, and process parameters [3]. Key material factors include porosity, fiber diameter, and material properties, all of which affect the available void space and flow resistance. Structural factors, such as pore geometry, fiber distribution, stacking sequence of layers, determine the pathways for resin flow. Higher compaction pressure and nesting within the structure reduce permeability. Fluid properties, such as viscosity and surface tension, also play a significant role, with higher viscosity increasing flow resistance [4]. Additionally, process parameters like pressure gradient, flow front velocity, and mold geometry impact resin distribution and flow uniformity. Defects such as voids, dry spots, and fiber misalignment further disrupt flow and decrease permeability [5]. Understanding and optimizing these parameters is essential for achieving consistent resin flow and improved quality of the final product.

Flow of liquid polymer (usually called resin) through a fiber reinforcement of a composite simultaneously occurs in two flow domains: intra-tow and inter-tow. Intra-tow flow occurs in between the fibers of a fiber bundle (a.k.a. tows) in a micro-scale, whereas inter-tow flow occurs between the fiber bundles in a meso-scale [6]. The dual scale nature of resin flow is important for determining overall permeability of a porous fiber reinforcement and investigating potential defects in a composite structure induced by dry spots (voids) remaining after mold filling. Intra-tow flow is significantly slower than the inter-tow flow due to lower intra-tow permeability, often leading to partial saturation and void formation in the intra-tow region [7]. Both intra- and inter-tow flow characteristics contribute to the overall permeability of a porous fiber reinforcement. Intra-tow and inter-tow flows are illustrated as in Figure 1.1.

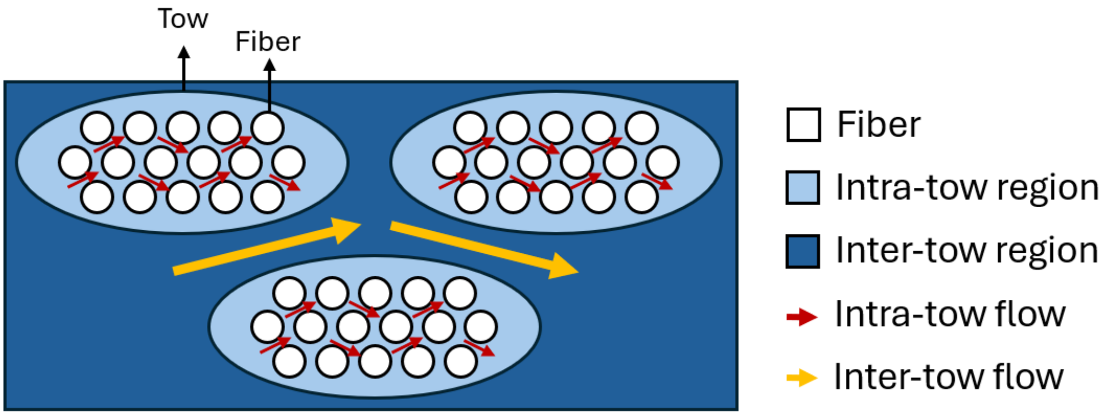

Figure 1.1: Intra-tow and inter-tow regions in a composite structure *[8]*

Intra-tow permeability was analytically studied by Gebart in 1992 [9]. For uniform quadratic and hexagonal fiber distributions, he derived an analytical relationship between permeability and radius of a fiber, r, and fiber volume fraction, V_f, for a flow parallel (along) and perpendicular (transverse) to the fibers. Figure 1.2 shows a unit cell of hexagonally distributed fibers. Formula for perpendicular permeability in a hexagonal fiber distribution, shown in Equation (1.2), will be used to validate the simulation results from ANSYS Fluent [9].

$$K_{\perp\, hex} = C_1 \left(\sqrt{\frac{V_{f,max}}{V_f}} - 1 \right)^{5/2} r^2 \tag{1.2}$$

C_1 is a constant, $K_{\perp\, hex}$ is permeability in the transverse direction to the fibers for a hexagonal fiber arrangement in the tow, r is the fiber radius, and V_f is the fiber volume fraction. For hexagonal fiber arrangement of tows, $C_1 = \frac{16}{9\pi\sqrt{6}}$ and maximum possible fiber volume fraction is $V_{f,max} = \frac{\pi}{2\sqrt{3}}$ [9].

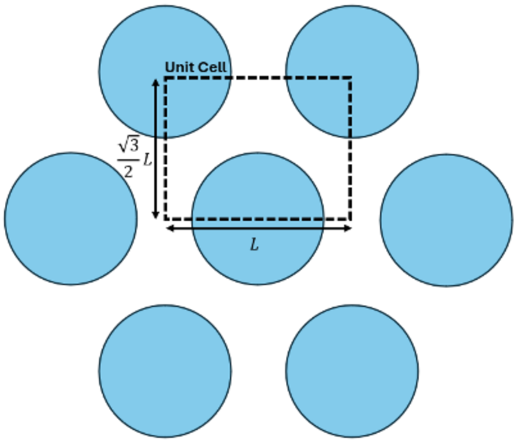

Figure 1.2: Unit cell of hexagonally distributed fibers *[9]*

1.3 Composite Manufacturing Modeling

Research on composite materials manufacturing modeling has demonstrated different permeability characterization approaches both experimentally and numerically. Experimental characterization and computational modeling serve as two complementary methodologies for process optimization and material behavior analysis.

Experimental modeling involves physically replicating manufacturing processes to directly measure material responses, such as resin flow and fiber orientation, under real-world conditions. While this method provides highly accurate data, it is often time-consuming, expensive, and limited in scale.

Flow front monitoring is one of the most used experimental methods which involves tracking the resin front as it progresses through the reinforcement material. This can be achieved by direct observation and digital image processing [10]. Another method involves using a flowmeter and pressure gauge to utilize Darcy's Law and correlate pressure differences with flow rates, providing an indirect but effective way to estimate permeability. Sensor-based and imaging-based methods employ non-invasive technologies that provide detailed information, using ultrasound, MRI (Magnetic Resonance Imaging), CT (Computed Tomography) scans to measure resin flow dynamics with precision and to reconstruct pore structures for permeability estimation [10].

Conventional experimental characterization procedures can result in a high margin of error. It is common to observe different research groups reporting permeability results that differ by an order of magnitude for the same fabric [11]. Even when issuing strict procedural guidelines, the margin of error remains as high as 25%. [12] Therefore, achieving consistency and accuracy in permeability characterization is of a paramount importance to the field.

On the other hand, computational modeling employs numerical techniques like finite element analysis (FEA) and computational fluid dynamics (CFD) to simulate the behavior of composite materials during various stages of manufacturing. This allows for the prediction of key factors such as thermal gradients, cure kinetics, and structural performance without the need for physical prototypes.

In permeability calculations, commercial CFD software has proven to be a useful tool for modelling various flow characteristics and domain sizes, significantly reducing the time and cost of experimental methods. Due to the high computational power required to model complex woven structures, the unit cell approach is adopted in many studies. A unit cell is the smallest representative and repetitive element which enables accurate modelling of the entire system [7]. An additional advantage of CFD is its capability to simulate flow at the micro-scale, a level not achievable experimentally, particularly for measuring intra-tow permeability [7].

1.4 Previous Studies on Composite Modeling

Considering the dual scale nature of resin flow, fiber reinforcement structures can be modeled as porous domains, where the fibers are treated as solid regions, and the space between them is considered a porous zone. Joemon et al. [13] proposed a method for numerically modeling the VARTM process by simulating resin flow in three-dimensional porous media using ANSYS Fluent. They calculated the time required for resin to fill the mold cavity under varying compaction pressures through computer simulation and validated their findings with experimental results [13]. Similarly, Alotaibi et al. investigated resin flow through a woven 3D unit cell in ANSYS Fluent, modeling the tows as porous zones with varying porosities. Their study examined the effects of tow curvature and intra-tow porosities on resin flow [7].

In another study, Tahir et al. defined fiber tows as porous zones in a two-dimensional flow domain in ANSYS Fluent. They achieved consistent results between two numerical models: one where the tows were modeled as porous zones and, another where tows were modeled as solid fibers. Their research explored how different parameters influence the overall permeability of a two-dimensional dual-scale fibrous structure using CFD [14].

Zhao et al. analyzed two-phase inter-tow and intra-tow flows for meso-scale void formation during mold filling. They developed a 3D unit cell of a woven structure in ANSYS Fluent, incorporating source terms through user defined functions (UDFs) to simulate resin flow [15]. In subsequent work, Alotaibi et al. similarly used UDFs in ANSYS Fluent to model resin flow, heat transfer, and chemical reactions, further enhancing the understanding of flow behavior in composite manufacturing processes [16].

Syerko et al. [17] presented a benchmark study in which real images of fiber tows were utilized for numerical modeling of the fiber reinforcement permeability. The models were created through image processing, and the study employed various CFD tools to simulate the same structure. This benchmark highlighted critical parameters affecting permeability determination, including boundary conditions, the number of subdomains, and the choice between 2D or 3D formulations [17].

In this research, the commercially available CFD software ANSYS Fluent is utilized for permeability calculation. The overall permeability of a fiber tow domain is computed by simulating the resin flow along a unit cell in ANSYS Fluent, where the fiber tows are modeled as porous zones. Various tow distribution scenarios are investigated, including manually created extreme cases and randomly generated cases using MATLAB. In each case, the distance between the adjacent tows perpendicular to the flow direction is varied to analyze significant flow channels or blockages and their impact on the overall permeability. An analogy between Darcy's Law and Ohm's Law is employed to predict the overall permeability of unidirectionally distributed porous fiber tows. The approximated and simulated permeabilities are compared, and the limitations of the approximation are examined by varying the domain size and intra-tow porosity. The major contribution of this study lies in its scalable and computationally efficient approximation method, which is applicable to various tow distributions and requires significantly less computational power and time.

Chapter 2:
SIMULATION OF FLOW TRANSVERSE TO INDIVIDUAL FIBERS

This chapter aims to calculate the permeability of a representative unit cell of fibers by using ANSYS Fluent. Results computed from ANSYS Fluent simulation are verified with permeability calculated from Gebart's relation in Equation (1.2).

2.1 Flow Domain

A representative unit cell is selected from a hexagonally distributed fiber geometry as shown in Figure 2.1. The fiber radius is chosen to be $2\mu m$, and the fibers are distributed in a uniform hexagonal pattern with a porosity value of 56.5%, which results in the domain dimensions of $11.5\mu m \times 10\mu m$. The geometry selected for the simulation does not represent the actual fiber dimensions, as the computational results are intended solely for analytical comparison. However, the domain is scalable if experimental comparisons are required. The selected unit cell consists of two complete fibers, two half fibers, and four quarter fibers, and it repeats periodically in both the x and y directions.

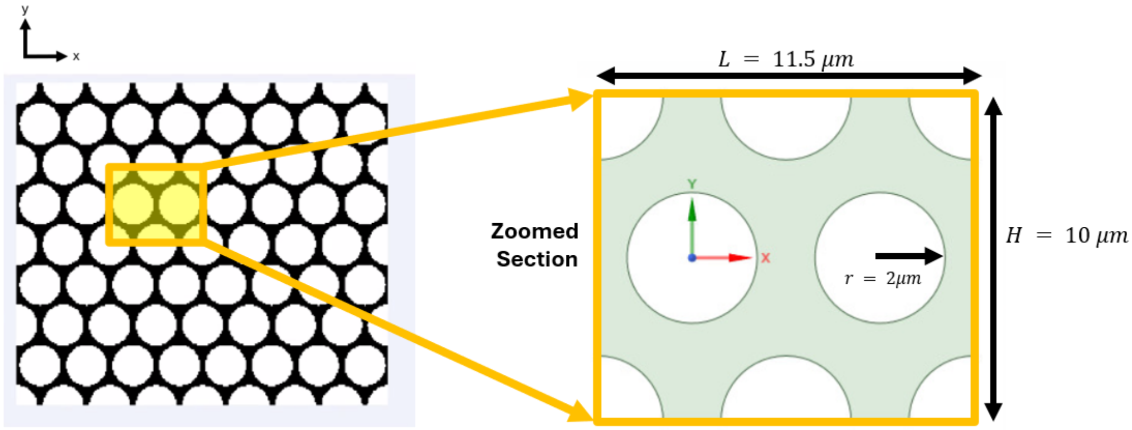

Figure 2.1: Selected representative unit cell for hexagonally distributed fibers

The fiber volume fraction of the domain is 43.5%, and the intra-tow porosity is 56.5%. Using the fiber volume fraction and fiber radius, the permeability of the domain is calculated as $1.21 \times 10^{-13}\ m^2$ by using Gebart's Equation (1.2). The details of Gebart's permeability calculation are provided in Appendix B.

Table 2.1: Parameters for unit cell of hexagonally distributed fiber domain

Parameter	Value
Domain Length (L)	11.5 µm
Domain Height (H)	10 µm
Fiber Radius (r)	2 µm
Intra-Tow Porosity (ϕ_t)	56.5%
Fiber Volume Fraction (V_f)	43.5%

2.2 *Flow Model and Boundary Conditions*

The flow model is steady-state, single-phase, laminar, and incompressible. The fluid is resin with a density of 1300 kg/m^3 and a viscosity of 0.15 $Pa \cdot s$. In the converged mesh model in Figure 2.2, there are 6634 quadrilateral elements and 6961 nodes. The mesh convergence graph is presented in Figure 2.3.

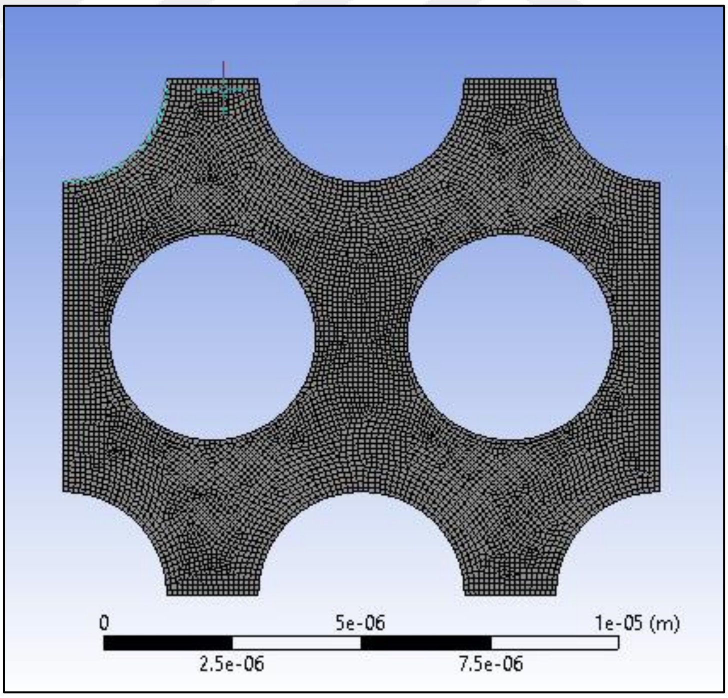

Figure 2.2: Mesh model for unit cell of hexagonally distributed fiber domain

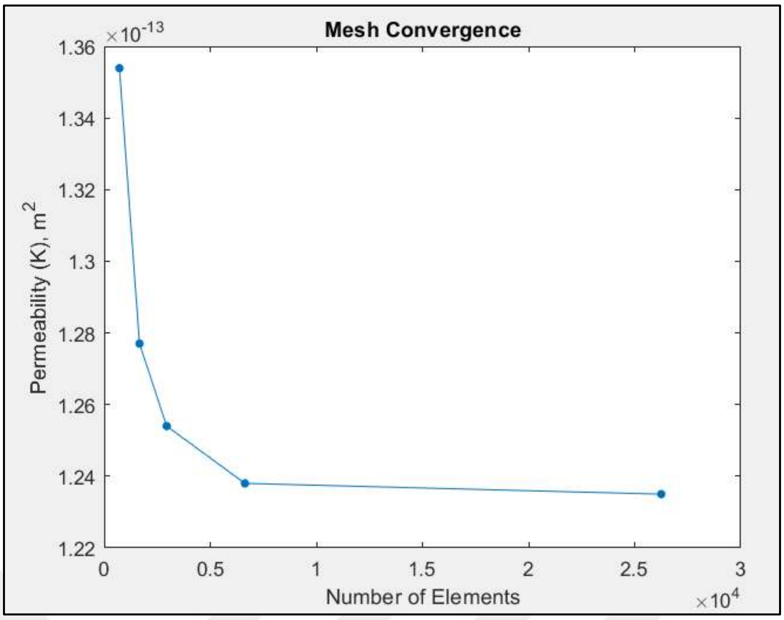

Figure 2.3: Mesh convergence for unit cell of hexagonally distributed fiber domain

The boundary conditions are illustrated in Figure 2.4.The left straight edge of the domain is set as a pressure inlet with a value of $10\ Pa$. The right straight edge is set as a pressure outlet with zero pressure creating a pressure gradient to enable resin flow from left to right. No-slip boundary condition is applied on the circular fiber interfaces. The top and bottom boundaries of the model are set as periodic boundaries, as the flow domain represents a unit cell which is repetitive in the y-direction.

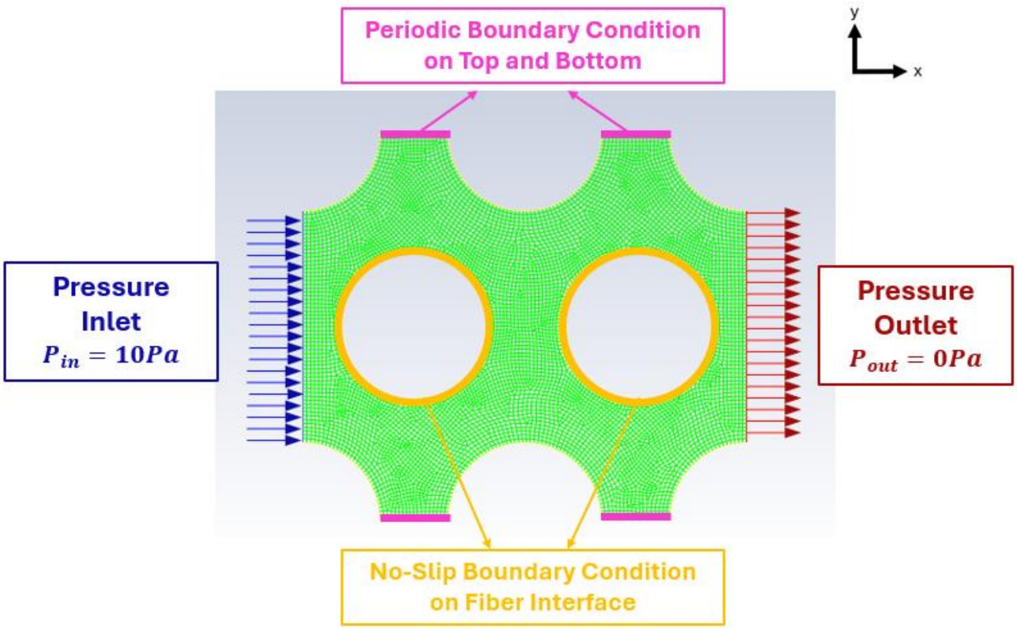

Figure 2.4: Boundary conditions for the unit cell of hexagonally distributed fibers

The model was solved by using the SIMPLE algorithm in ANSYS Fluent, employing least-square cell discretization for gradient computation, second-order discretization for pressure, and second-order upwind discretization for momentum.

2.3 *Permeability Calculation*

The volumetric flowrate of the resin in the inlet is obtained from Fluent. For the overall permeability calculation along the unit cell, Darcy's Law is applied. Darcy's Law for flow in x-direction is expressed in Equation (2.1) [2].

$$u_x = -\frac{K_x}{\mu}\frac{\partial P}{\partial x} \tag{2.1}$$

To find the volumetric flow rate along the inlet, it is integrated along the inlet edge (from 0 to H).

$$Q_{inlet} = \int_0^H u_x Z dy = -\frac{K_x HZ}{\mu}\frac{\partial P}{\partial x} \tag{2.2}$$

$$Q_{inlet} = -\frac{K_x HZ}{\mu}\frac{\partial P}{\partial x} \tag{2.3}$$

The pressure gradient along the x-direction $\left(\frac{\partial P}{\partial x}\right)$, viscosity of the resin (μ), and domain height (H) are known. Volumetric flowrate of the inlet (Q_{inlet}) is obtained from ANSYS Fluent. Domain thickness (Z) is assumed to be $1\,m$ for 2D ANSYS Fluent models. The overall permeability (K_x) is computed from Equation (2.3). A sample calculation is shown in Appendix C.

As Gebart's equation is valid for flow transverse to fibers, the permeability for flow in both x- and y-directions is expected to be the same. Therefore, simulations for both x-direction and y-direction flow are performed in ANSYS for the same domain. $K_{\perp,x}$ and $K_{\perp,y}$ are computed for the cases shown in Figure 2.5 (a) and (b), respectively.

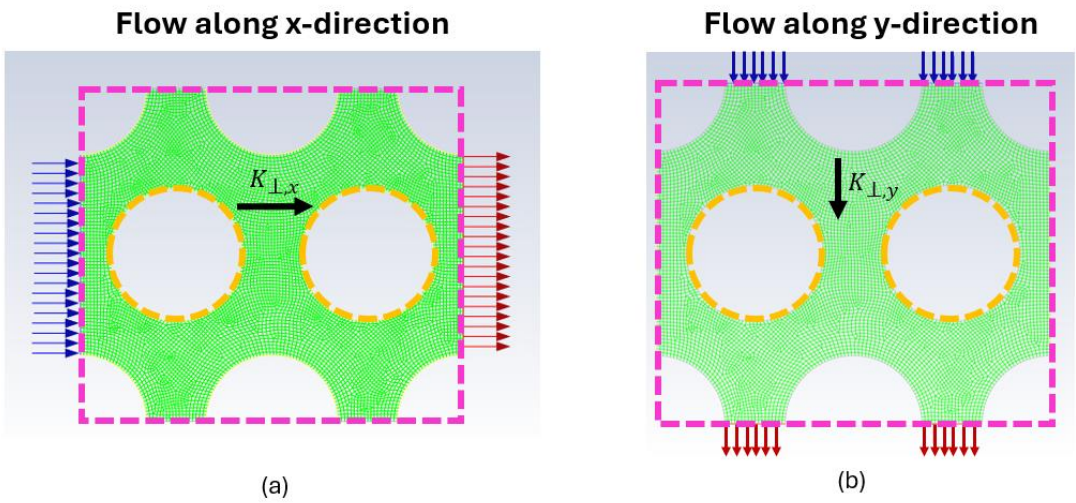

Figure 2.5: Flow models for (a) flow in the x-direction and (b) flow in the y-direction

Permeability values calculated by ANSYS Fluent and those from Gebart's formula are shown in Table 2.2. The values correlate well, with percentage errors of 2.48% and 1.65% for $K_{\perp,x}$ and $K_{\perp,y}$, respectively.

Table 2.2: Permeability comparison for results from ANSYS Fluent simulations and Gebart's analytical formula

Permeability Calculated by ANSYS Fluent		**Permeability Calculated by Gebart's Formula**
$\mathbf{K}_{\perp,x}$ $[m^2]$	$\mathbf{K}_{\perp,y}$ $[m^2]$	$\mathbf{K}_{\perp,Gebart}$ $[m^2]$
1.24×10^{-13}	1.23×10^{-13}	1.21×10^{-13}

For further verification of the model, the representative unit cell in Figure 2.1 is divided into three additional unit cells, as shown in Figure 2.6. Similar to the calculations for Unit Cell A, simulations are conducted for flow in x- and y-directions for Unit Cells B, C and D. Permeability values of all unit cells in both directions are summarized in Table 2.3. As all unit cells represent the same hexagonal fiber distribution with the same porosity and flow parameters, they are expected to yield the same permeability results. Table 2.4 provides the percentage errors for each case. Maximum percent error is found to be 3.31% which is acceptable given the modelling limitations and assumptions, such as mesh model, boundary conditions, discretization schemes and numerical algorithms.

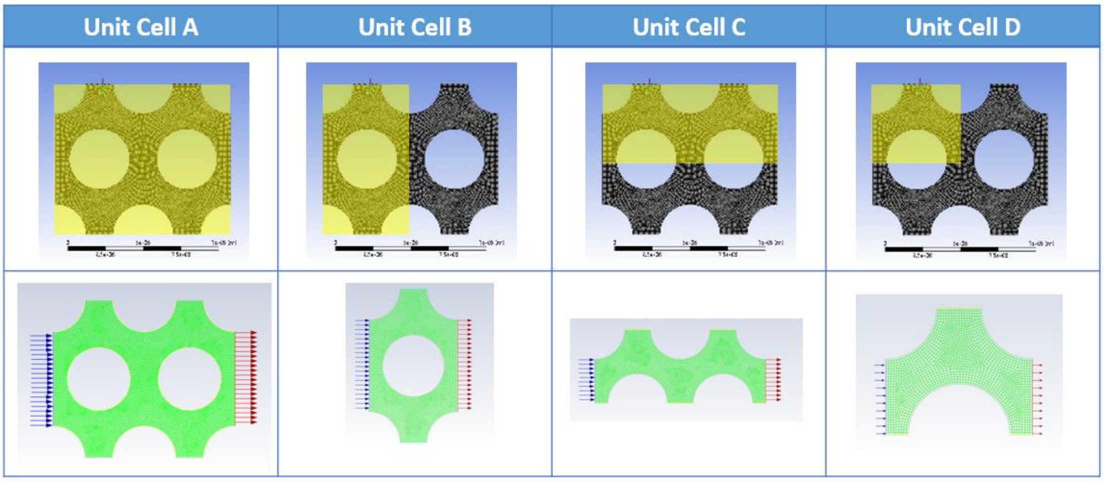

Figure 2.6: Different unit cells for hexagonally distributed fibers

Table 2.3: Permeability comparison for Unit Cells A, B, C and D

Unit Cell	Permeability Calculated by ANSYS Fluent		Permeability Calculated by Gebart's Formula
	$K_{\perp,x}$ $[m^2]$	$K_{\perp,y}$ $[m^2]$	$K_{\perp,Gebart}$ $[m^2]$
A	1.24×10^{-13}	1.23×10^{-13}	1.21×10^{-13}
B	1.25×10^{-13}	1.23×10^{-13}	
C	1.24×10^{-13}	1.22×10^{-13}	
D	1.25×10^{-13}	1.22×10^{-13}	

Table 2.4: Percent errors for permeabilities of Unit Cells A, B, C and D

Unit Cell	Percent Error	
	For $K_{\perp,x}$	For $K_{\perp,y}$
A	2.48%	1.65%
B	3.31%	1.65%
C	2.48%	0.83%
D	3.31%	0.83%

It can be concluded that the ANSYS Fluent model aligns well with Gebart's analytical solution. Among the eight permeability results for the four unit cells, the mean permeability is $1.24 \times 10^{-13}\ m^2$, with a standard deviation of $1.20 \times 10^{-15}\ m^2$.

Chapter 3:
SIMULATION OF FLOW TRANSVERSE TO UNIDIRECTIONAL TOWS

3.1 Flow Domain

Two-dimensional resin flow transverse to a fiber tow domain is simulated using ANSYS Fluent. The flow domain is designed as a two-dimensional region comprising uniformly distributed fiber tows, as illustrated in Figure 3.1. The domain represents a repeating unit cell of unidirectional tows in a composite structure. The dark blue region represents the empty space where resin can flow freely, while the light blue areas represent the fiber tows with a defined intra-tow porosity. The fiber tows are assumed to have an elliptical shape, reflecting the elongation of individual fibers in x-direction due to the layered and compacted structure of the composite preform.

The dimensions of the model are shown in Figure 3.2, and input parameters are presented in Table 3.1. The tows are arranged in a uniform pattern, with equal spacing between adjacent tow centers in both the x- and y-directions. Each tow is assumed to be identical to the other in terms of size and porosity. The domain does not include inlet or outlet pools to represent a repeating unit cell. Comparison of the domain with inlet and outlet pools will be discussed in Section 3.4.

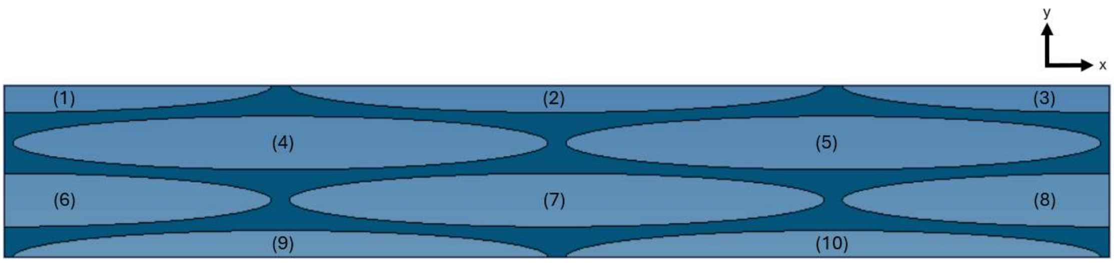

Figure 3.1: Flow domain of unidirectionally distributed 10 fiber tows

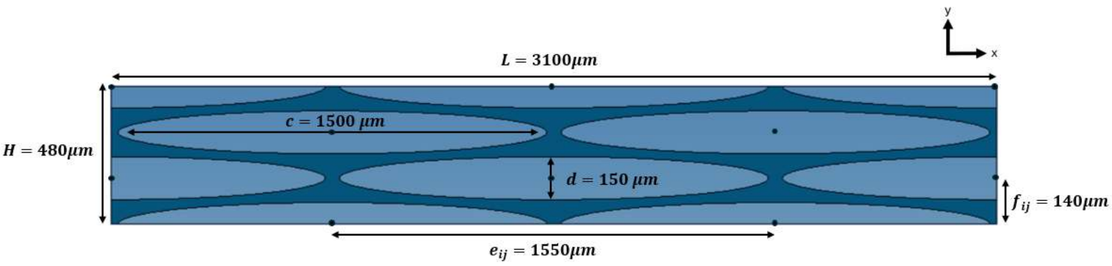

Figure 3.2: Flow domain geometry for the nominal case of unidirectionally distributed 10 fiber tows

Table 3.1: Domain parameters for the nominal case of unidirectionally distributed 10 fiber tows

Parameters	Value
Domain length (L)	$3100 \mu m$
Domain height (H)	$480\ \mu m$
Major axis of tows (c)	$1500\ \mu m$
Minor axis of tows (d)	$150\ \mu m$
x-distance between adjacent tow centers (e)	$1550\ \mu m$
y-distance between adjacent tow centers (f)	$140\ \mu m$
Inter-tow porosity (ϕ_s)	29%
Intra-tow porosity (ϕ_t)	50%
Overall porosity (ϕ_o)	64%
Fiber radius (r)	$5\ \mu m$

3.2 *Flow Model and Boundary Conditions*

The flow model is steady-state, single-phase, laminar, and incompressible. The fluid used in the simulation is resin, with a density of 1300 kg/m^3 and a viscosity of 0.15 $Pa.s$. Two fluid zones are defined in the domain: the tows are modeled as porous zones, while the space between the tows is modeled as an empty zone where the resin can flow freely. Each porous zone is characterized by an intra-tow porosity and viscous resistance. Intra-tow porosity is defined to be 50% for each fiber tow. The viscous resistance is the inverse of absolute permeability [18].

Intra-tow permeability is calculated by using Gebart's formula in Equation (1.2) as $4.09 \times 10^{-13}\ m^2$ for a fiber radius of $5\ \mu m$. The corresponding viscous resistance is calculated as $2.45 \times 10^{12}\ m^{-2}$, that is a required input to model a porous zone in ANSYS Fluent. Modeling tows as porous zones rather than individual fibers significantly reduces computational load.

Boundary conditions of the domain are shown in Figure 3.3. The left edge of the domain is set as a pressure inlet with 1 kPa while the right edge is set as pressure outlet with zero pressure, creating a pressure gradient to enable resin flow from left to right. The boundaries between the porous and the empty zones are defined as interfaces. The upper and lower edges of the model are set as symmetric boundaries because the upper and lower boundaries do not match for defining a periodic structure. The upper boundary contains three tows, whereas the lower boundary contains two tows.

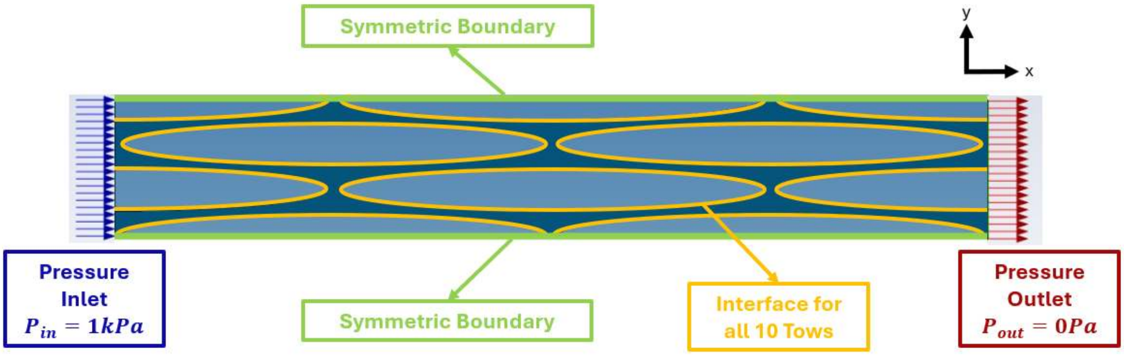

Figure 3.3: Boundary conditions for tow domain

Figure 3.4 shows the boundary conditions and the corresponsing governing equations of unidirectionally distributed 10 fiber tows.

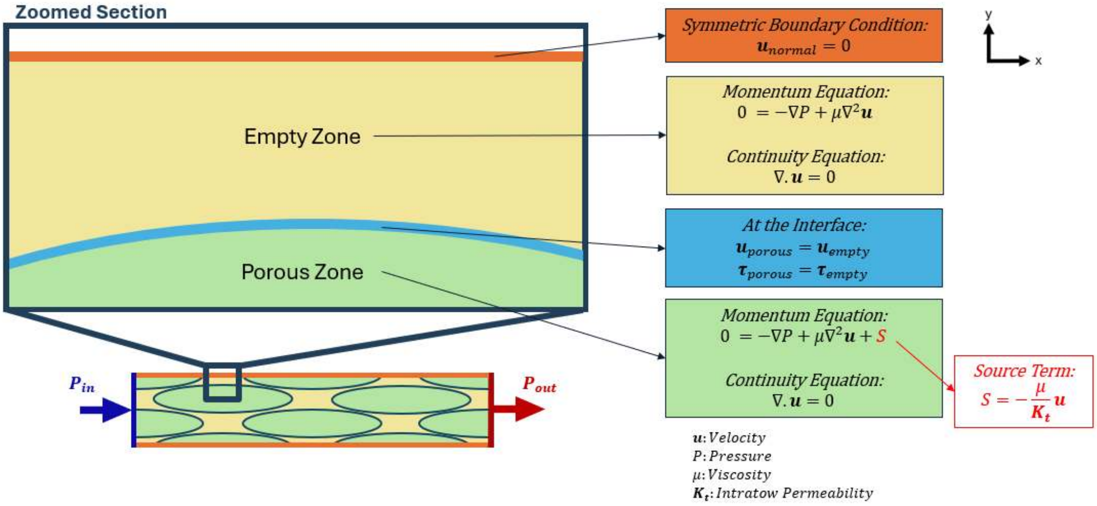

Figure 3.4: Boundary conditions and governing equations of tow domain

The model was solved by using the SIMPLE algorithm in ANSYS Fluent. The method is chosen as least-square cell discretization for gradient computation, second-order discretization for pressure, and second-order upwind discretization for momentum.

In a flow channel, the fluid flow is defined by mass and momentum equations, shown as in Equation (3.1) and (3.2).

$$\frac{\partial \rho}{\partial t} + \nabla . (\rho \boldsymbol{u}) = 0 \tag{3.1}$$

$$\frac{\partial}{\partial t}(\rho \boldsymbol{u}) + \nabla . (\rho \boldsymbol{u} \boldsymbol{u}) = -\nabla P + \mu \nabla^2 \boldsymbol{u} + \rho \boldsymbol{g} \tag{3.2}$$

ρ is density, t is time, $\boldsymbol{u}$ is the velocity vector, P is pressure, μ is viscosity and $\boldsymbol{g}$ is gravitational acceleration.

The effect of intra-tow permeability is represented by adding a source term S to Equation (3.2) as below in Equation (3.2).

$$\frac{\partial}{\partial t}(\rho \boldsymbol{u}) + \nabla.(\rho \boldsymbol{u}\boldsymbol{u}) = -\nabla P + \mu \nabla^2 \boldsymbol{u} + \rho \boldsymbol{g} + S \tag{3.3}$$

The source term is defined in Equation (3.4).

$$S = -\frac{\mu}{K_t}\boldsymbol{u} \tag{3.4}$$

K_t is the intra-tow permeability and $1/K_t$ represents the viscous resistance which is a required input in the porous zone definition of ANSYS Fluent [18].

The flow is assumed to be incompressible and in a steady state with no inertial or gravitational acceleration, so the governing equations simplify as below.

$$\nabla.\boldsymbol{u} = 0 \tag{3.5}$$

$$0 = -\nabla P + \mu \nabla^2 \boldsymbol{u} - \frac{\mu}{K_t}\boldsymbol{u} \tag{3.6}$$

3.3 Fluent SIMPLE Solver

The SIMPLE (Semi-Implicit Method for Pressure-Linked Equations) solver is a pressure-based segregated solver that solves pressure and momentum equations sequentially based on a prediction and correction approach. The SIMPLE solver in Fluent is used in this study because coupled solvers require more memory and are not compatible with periodic flows [18].

In the SIMPLE algorithm, a relationship between velocity and pressure is utilized to determine the pressure field by using the conservation of mass. At first, the momentum equation is solved with the initial pressure condition.

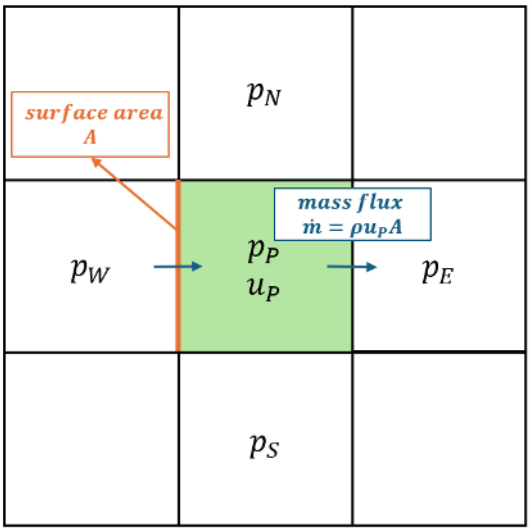

Figure 3.5: Discretized unit cell for momentum equation

Figure 3.5 represents a discretized unit cell where a pressure difference and a mass flux are defined. The discretized momentum equation is expressed as Equation (3.7).

$$a_P u - \sum_{nb} a_{nb} u_{nb} = A(p_W^* - p_E^*) \tag{3.7}$$

Here, nb represents neighboring grid point (e.g., E for east). $a_P u_P - \sum_{nb} a_{nb} u_{nb}$ is the net momentum flux for cell P and $A(p_W^* - p_E^*)$ is the pressure force. A relation between the change in velocity and the change in pressure can be derived from Equation (3.7) as shown in Equation (3.8).

$$u_P' = \frac{\sum_{nb} a_{nb} u_{nb}'}{a_P} + d_P(p_W - p_E), \text{ where } d_P = \frac{A}{a_P} \tag{3.8}$$

By neglecting $\sum_{nb} a_{nb} u_{nb}'$, the velocity correction term simplifies to Equation (3.9).

$$u_P' = d_P(p_W - p_E) \tag{3.9}$$

The second step is to apply the conservation of mass to the cell. Equation (3.10) represents the net mass flux, which is the sum of the current velocity (u^*) and the correction velocity (u'). The net mass flux should be equal to zero to satisfy the conservation of mass.

$$0 = \sum_{nb} \rho u_{nb}^* A + \sum_{nb} \rho u_{nb}' A \tag{3.10}$$

Therefore, the correction mass flux equals the negative of the current mass flux. For the representative cell in Figure 3.5, Equation (3.10) can be rewritten as Equation (3.11).

$$(\rho u' A)_e - (\rho u' A)_w + \cdots = -\dot{m}^* \tag{3.11}$$

Combining Equation (3.11) and (3.9), the equation can be written in terms of pressure, as in Equation (3.12).

$$(\rho A d)_e (p'_P - p'_E) - (\rho A d)_w (p'_W - p'_P) + \cdots = -\dot{m}^* \tag{3.12}$$

The pressure correction equation is then simplified from the discretized momentum equation into Equation (3.13).

$$a_P p'_P - \sum_{nb} a_{nb} p'_{nb} = -\dot{m}^* \tag{3.13}$$

Equation (3.13) is the pressure correction equation for the iterative solution. Pressure and velocity are corrected iteratively using Equations (3.14) and (3.15).

$$p_P \rightarrow p^*_P + p'_P \tag{3.14}$$

$$u_P \rightarrow u^*_P + d_P (p'_W - p'_E) \tag{3.15}$$

Both mass and momentum equations must satisfy a convergence criterion. In most cases, the velocity result does not satisfy the mass conservation equation in first calculation step. The correction process is repeated iteratively until convergence is achieved within a predefined error tolerance. As a result, velocity and pressure distributions of the flow domain are obtained.

From the computed velocity field, the volumetric flow rate at the inlet is obtained from ANSYS Fluent. Darcy’s Law is then applied to calculate the overall permeability along the domain following the same approach explained in Section 2.3 and detailed further in Appendix C.

The mesh model is generated by quadrilateral elements. To ensure accuracy of the solution, a mesh convergence study is conducted. The same simulation is run for different mesh sizes, and the computed overall permeability values are compared. Based on the mesh convergence study shown in Figure 3.7, a mesh model with 375633 quadrilateral elements and 386152 nodes is selected for the study. The mesh model is shown in Figure 3.6.

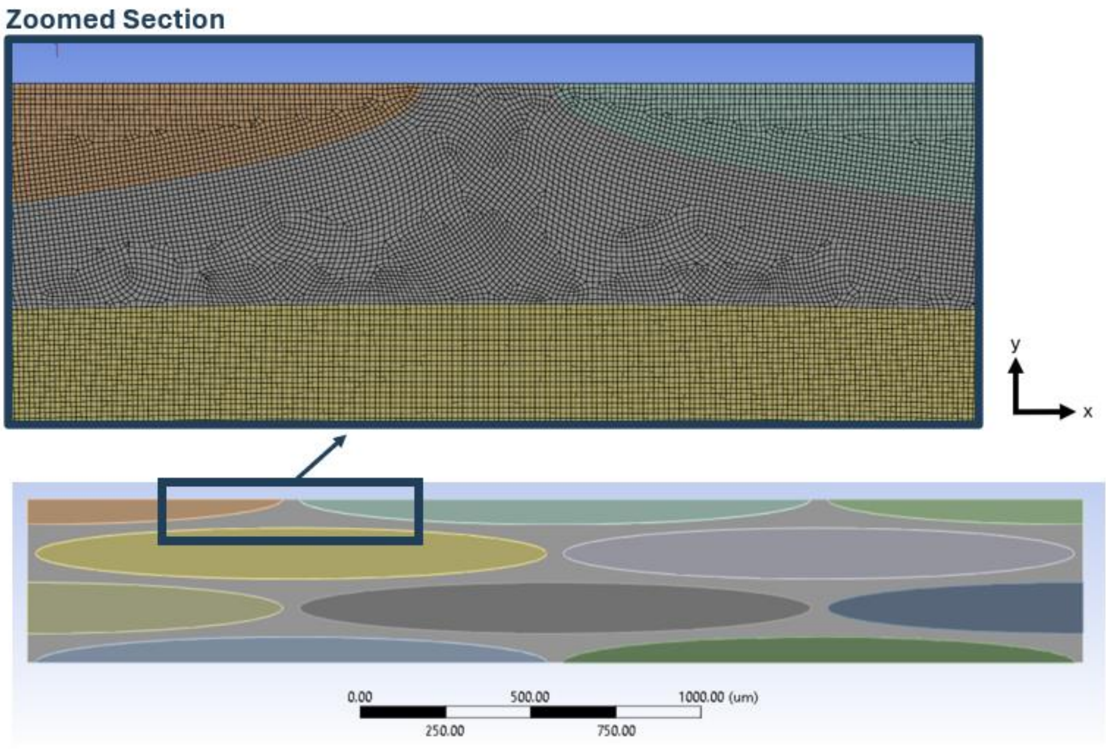

Figure 3.6: Mesh model of tow domain

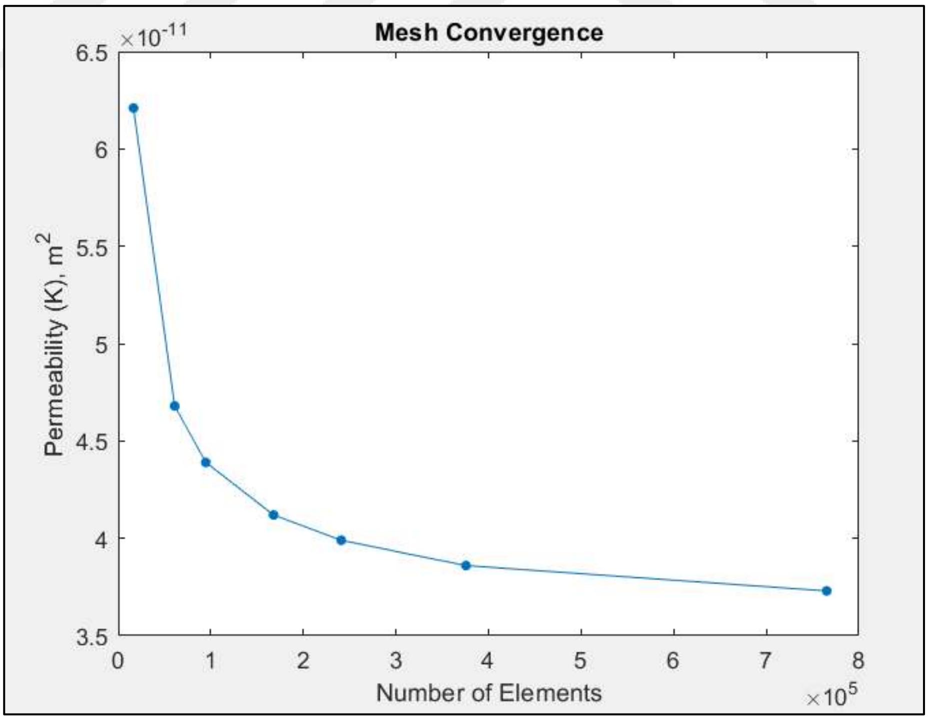

Figure 3.7: Mesh convergence for tow domain

3.4 *Effect of Inlet and Outlet Pools*

As shown in Figure 3.1, the flow domain is not modeled with an inlet and an outlet pool. Inlet and outlet pools are usually used to ensure the flow to evenly disperse. Initially, the model is created as shown in Figure 3.8(a). When it is solved, it is observed that there is no significant change in the pressure until the resin reaches tow #4 and #9 at $x = 950\ \mu m$. Similarly, there is almost no change in pressure after tows #5 and #10 in the outlet at $x = 4050\ \mu m$. Figure 3.9 shows (a) the pressure distribution, and (b) pressure graph for the case with inlet and outlet pools.

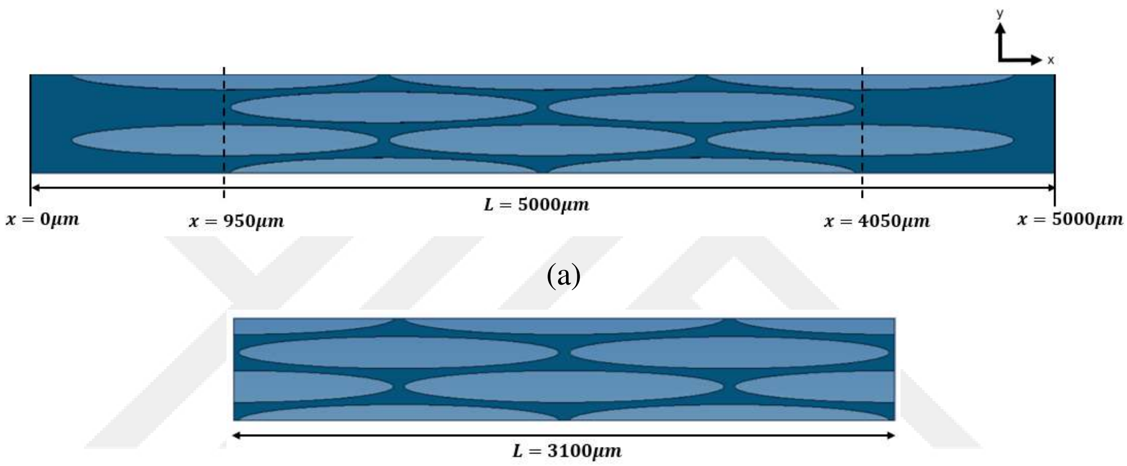

(b)

Figure 3.8: Tow domain (a) with inlet and outlet pools and (b) without inlet and outlet pools

(a)

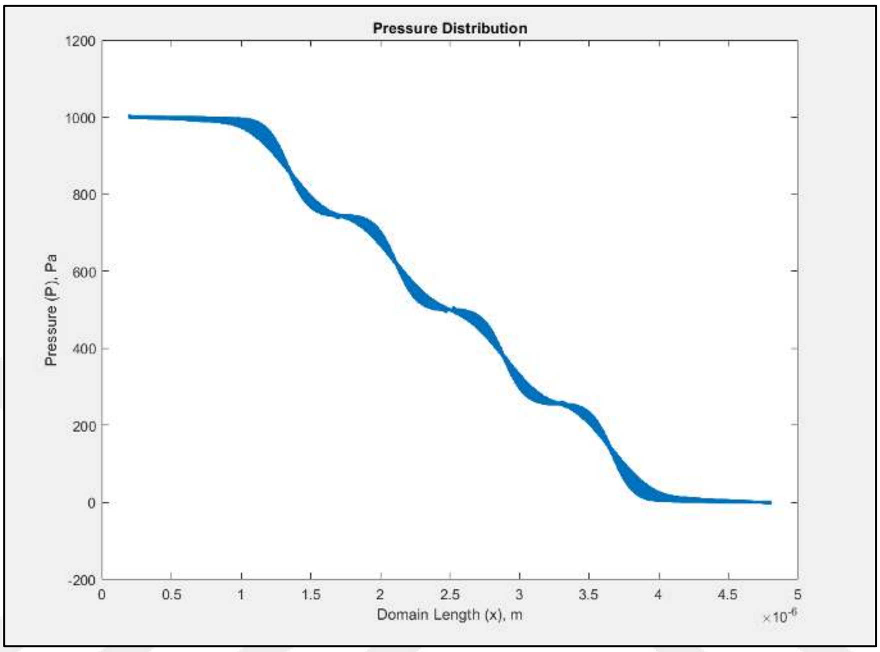

(b)

Figure 3.9: (a) Pressure distribution and (b) pressure vs x-position for tow domain with inlet and outlet pools

The pressure is observed to be changing in y-direction as well. Therefore, the pressure plot in Figure 3.9(b) is not linear. This occurs due to the resistance of the porous tows to the pressure change. When the resin flow reaches the tows, there is a pressure distribution along the y-axis because the pressure inside the tow and the pressure between tows are not equal. The pressure inside the tow decreases slower than the pressure between the tows.

Figure 3.10 shows the velocity and pressure distribution when the pools are removed from the domain as shown in Figure 3.8(b). The pressure distribution exhibits a constant decrease in the pressure with no steady regions at the inlet and outlet.

(a)

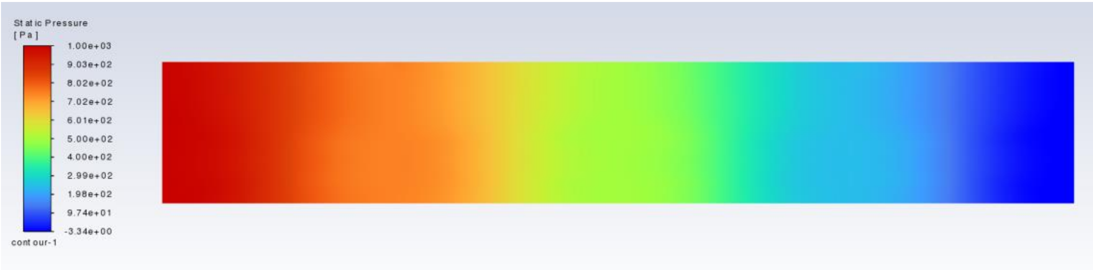

(b)

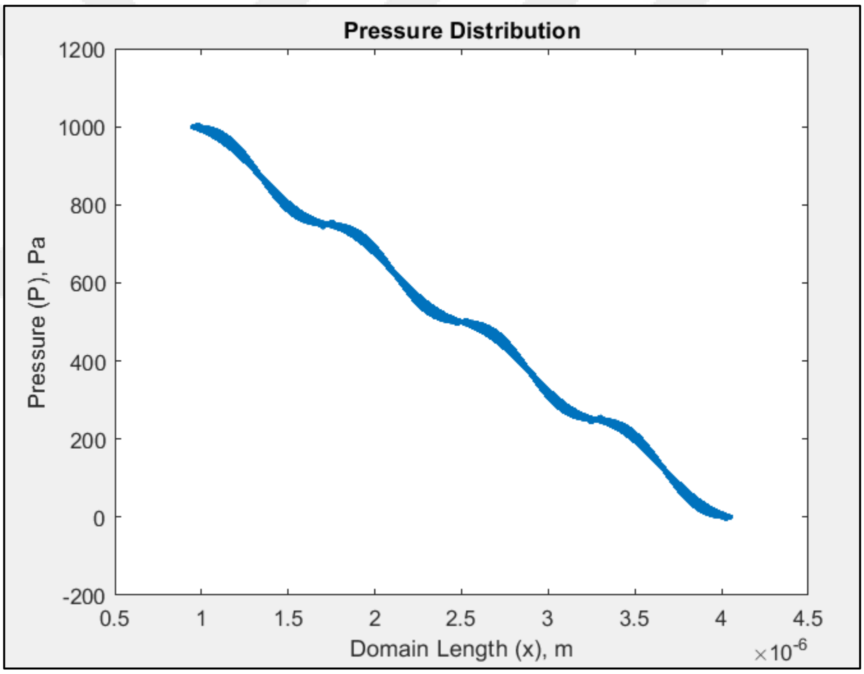

(c)

Figure 3.10: (a) Velocity distribution (b) pressure distribution and (c) pressure vs x-position for tow domain without inlet and outlet pools

Comparison of the results is shown in Table 3.2. There is a significant difference between the two overall permeabilities with a ratio of 1.60 ($K_{o,pool}/K_o$). Even though the inlet flow rates are similar, the overall permeability are different because when there are no inlet or outlet pools, the resin flows with difficulty and permeability decreases. The difference shows that the pools prevent representation of repetitive unidirectional tows.

Table 3.2: Permeability comparison for tow domains with and without pools

Domain Length $(\boldsymbol{L})$ $[\boldsymbol{\mu m}]$	**Pressure Inlet** $(\boldsymbol{P_{inlet}})$ $[\boldsymbol{kPa}]$	**Pressure Outlet** $(\boldsymbol{P_{outlet}})$ $[\boldsymbol{kPa}]$	**Calculated Volumetric Flowrate from ANSYS** $(\boldsymbol{Q_{inlet}})$ $[\boldsymbol{m^3/s}]$	**Calculated Overall Permeability from** $\boldsymbol{Q_{inlet}}$ $(\boldsymbol{K_o})$ $[\boldsymbol{m^2}]$
5000	1	0	0.395×10^{-7}	0.617×10^{-10}
3100	1	0	0.399×10^{-7}	0.386×10^{-10}

3.5 100 Randomly Distributed Tow Cases

A statistical variation is applied to the tow configuration in the domain geometry depicted in Figure 3.8(a), where there are inlet and outlet pools. The domain without pools will be used in further studies, however, this statistical study gives an insight to random distribution of the tows. Both x- and y-distances between adjacent tows are varied randomly by keeping domain size the same. A total of 100 different geometries are created by assigning random values to tow distances in MATLAB. The geometry is then imported to ANSYS Fluent by using the parameter feature of ANSYS Workbench.

Domain parameters (L, H, c, d, i, j) are fixed, whereas (e, f) are independent parameters defined as random numbers in MATLAB. The points y_1, y_2, y_3 are fixed on the upper boundary of the randomly created domain due to the symmetry constraint. Similarly, y_9 and y_{10} are fixed on the bottom boundary of the randomly created domain due to the same constraint. There is a no-touch condition between tows to avoid the generation of poor-quality mesh elements.

Calculated overall permeabilities are presented in a scatter diagram in Figure 3.11. It is observed that 98% of the overall permeability results are lower than the overall permeability of the nominal case. There are two cases where the overall permeability is higher than the nominal case. This indicates that a sample size of 100 is insufficient to represent cases where the tows have larger distance between each other, allowing resin to flow through the tows more easily. Figure 3.12 shows a histogram for 100 random case results, indicating that more than 25% of the cases have permeabilities between

$5.8 \times 10^{-11}\ m^2$ and $5.9 \times 10^{-11}\ m^2$. The mean value for overall permeability is calculated to be $5.90 \times 10^{-11}\ m^2$ with a standard deviation of $1.65 \times 10^{-12}\ m^2$.

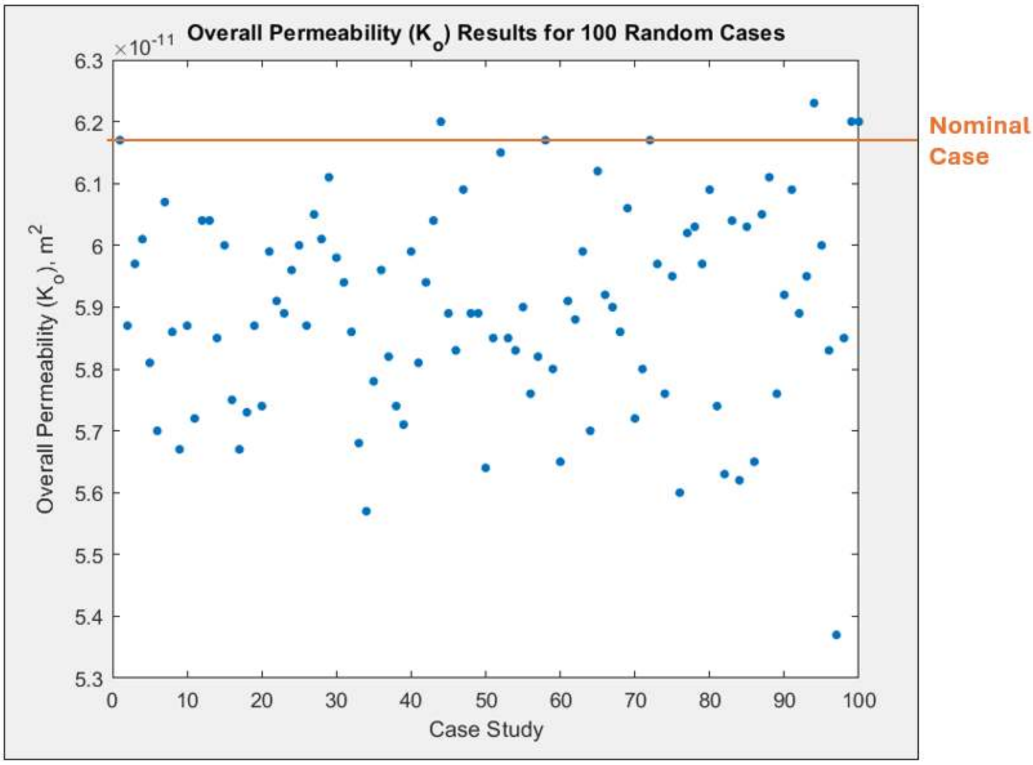

Figure 3.11: Overall permeability results of 100 random cases

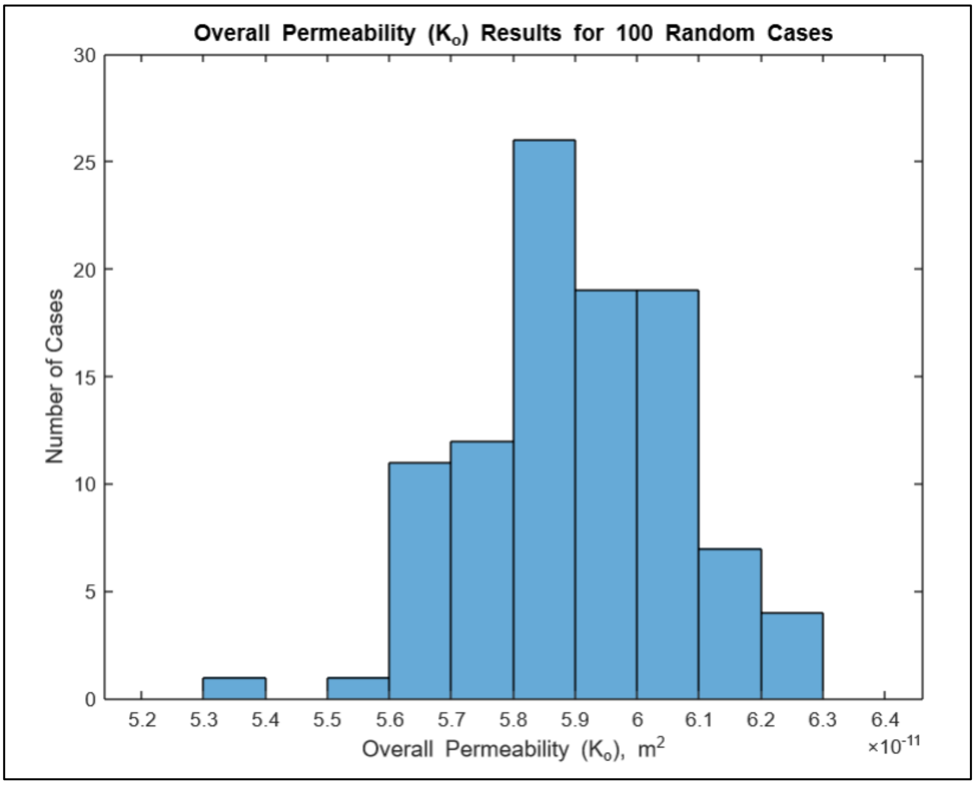

Figure 3.12: Histogram for overall permeability results of 100 random cases

Channel gap (h) is defined as the minimum distance in the y-direction between two elliptical tows as illustrated in Figure 3.13.

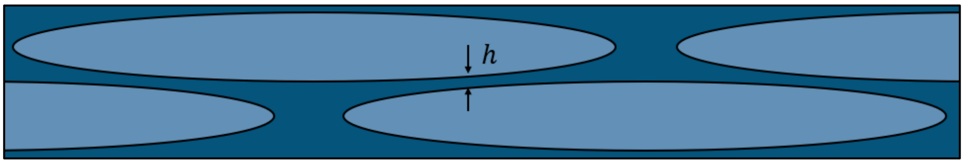

Figure 3.13: Channel gap (h) between tows

The overall permeabilities of 100 random cases are compared with average, minimum and maximum channel gaps between the elliptical tows in Figure 3.14(a), (b), and (c), respectively. From Figure 3.14(a), the average channel gap is observed to be the same for all simulations since the domain size is kept at $5000\ \mu m \times 480\ \mu m$ and the tow dimensions are not varied.

In Figure 3.14(b), there is no direct correlation observed between the minimum channel gap and overall permeability. This could be due to the minimum channel gaps representing the blockage points of the flow, but it fails to represent the channels where the flow is dominant and can easily pass through. The dominant channels likely have the most significant effect on the overall permeability of the domain since most of the resin would flow through these channels, making the channels with minimum gaps negligible.

Among the graphs for average, minimum and maximum gaps, the strongest relationship is observed between overall permeability and the maximum channel gap. Even though there is no direct correlation, a trend can be observed indicating as the maximum channel gap increases, the overall permeability also increases as shown in Figure 3.14(c). However, the sample size of 100 case studies may not be sufficient to represent this trend conclusively, as it may fail to capture extreme cases where the permeability is higher than the nominal case.

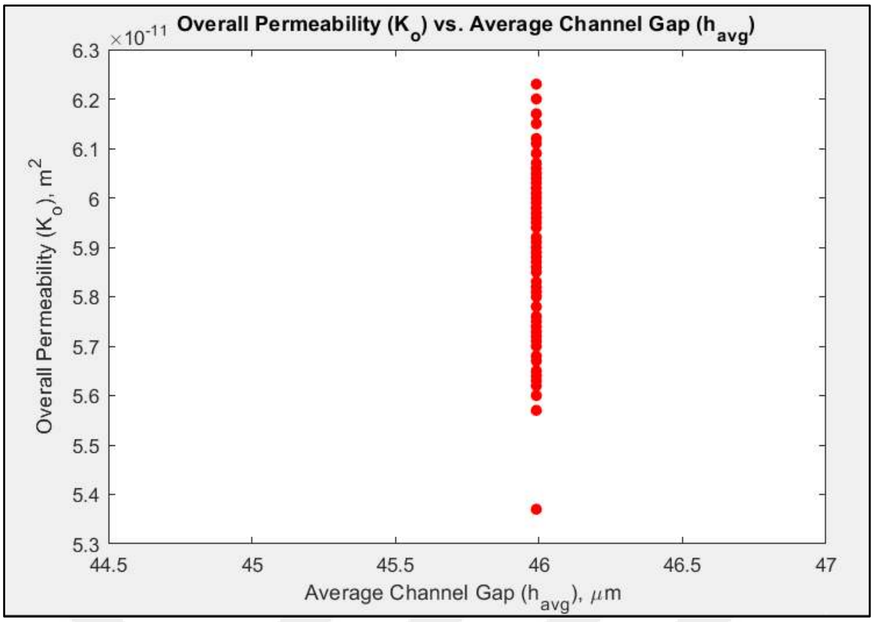
Overall Permeability (K_o) vs. Average Channel Gap (h_{avg})
$\times 10^{-11}$
6.3
6.2
6.1
6
5.9
5.8
5.7
5.6
5.5
5.4
5.3
Overall Permeability (K_o), m^2
44.5
45
45.5
46
46.5
47
Average Channel Gap (h_{avg}), μm

(a)

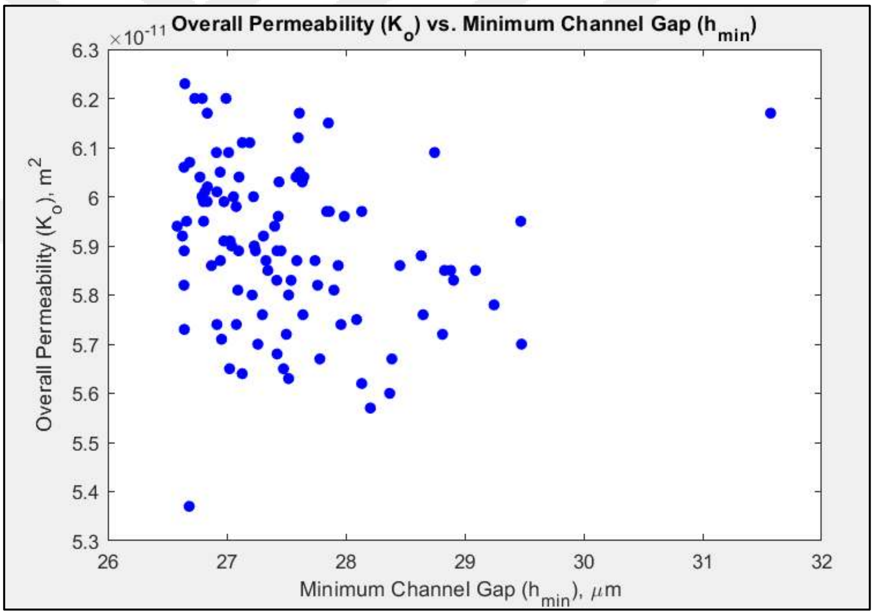
Overall Permeability (K_o) vs. Minimum Channel Gap (h_{min})
$\times 10^{-11}$
6.3
6.2
6.1
6
5.9
5.8
5.7
5.6
5.5
5.4
5.3
Overall Permeability (K_o), m^2
26
27
28
29
30
31
32
Minimum Channel Gap (h_{min}), μm

(b)

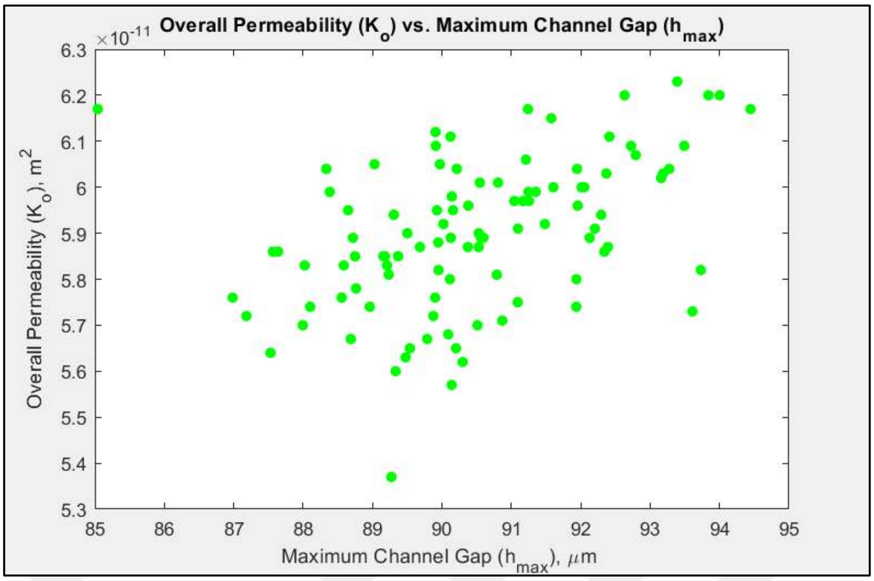

(c)

Figure 3.14: Overall permeability versus (a) average, (b) minimum, and (c) maximum channel gaps for 100 random cases

3.6 Extreme Cases

As 100 sample cases are insufficient to represent different channel flow scenarios, six additional extreme cases are analyzed using ANSYS Fluent. The extreme geometries are modeled by manually adjusting the distances between tows. Tow positions remain fixed along the x-axis. Only tows #4, #5, #6, #7 and #8 are moved in y-axis, assuming that tows #1, #2, #3, #9 and #10 are fixed. The variations in tow center positions relative to the nominal configuration are presented in Table 3.3.

Table 3.3: Tow center variation for extreme cases in μm

Cases	Tow 1	Tow 2	Tow 3	Tow 4	Tow 5	Tow 6	Tow 7	Tow 8	Tow 9	Tow 10
1	(0,0)	(0,0)	(0,0)	(0,0)	(0,0)	(0,0)	(0,0)	(0,0)	(0,0)	(0,0)
2	(0,0)	(0,0)	(0,0)	(0,+20)	(0,+20)	(0,+40)	(0,+40)	(0,+40)	(0,0)	(0,0)
3	(0,0)	(0,0)	(0,0)	(0,+20)	(0,+20)	(0,-20)	(0,-20)	(0,-20)	(0,0)	(0,0)
4	(0,0)	(0,0)	(0,0)	(0,-40)	(0,-40)	(0,-20)	(0,-20)	(0,-20)	(0,0)	(0,0)
5	(0,0)	(0,0)	(0,0)	(0,+20)	(0,+20)	(0,-20)	(0,-20)	(0,+40)	(0,0)	(0,0)
6	(0,0)	(0,0)	(0,0)	(0,+20)	(0,+20)	(0,-20)	(0,+40)	(0,-20)	(0,0)	(0,0)
7	(0,0)	(0,0)	(0,0)	(0,-10)	(0,+20)	(0,+10)	(0,-20)	(0,+40)	(0,0)	(0,0)

The velocity distributions of each case are shown in Figure 3.15. Volumetric flow rate and overall permeability values computed from ANSYS simulation results are tabulated in Table 3.4.

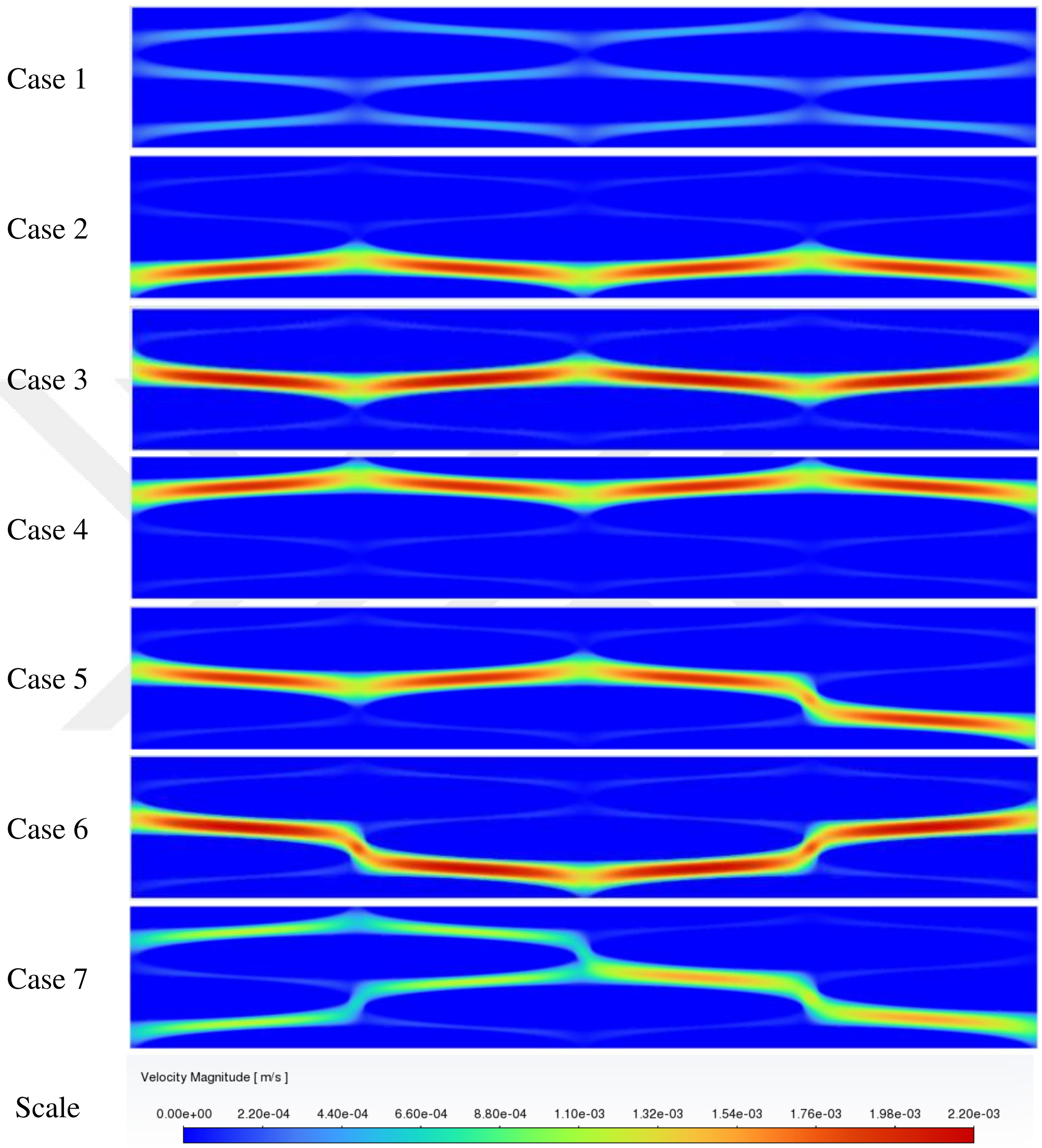

Figure 3.15: Velocity distribution graphs for the nominal and six extreme cases

Table 3.4: Volumetric flow rate and overall permeability results of the nominal and six extreme cases

Case	Calculated Volumetric Flowrate from ANSYS $Q_{inlet}[m^3/s]$	Calculated Overall Permeability from Q_{inlet} $K_o[m^2]$
1	0.399×10^{-7}	0.386×10^{-10}
2	1.08×10^{-7}	1.05×10^{-10}
3	1.08×10^{-7}	1.05×10^{-10}
4	1.08×10^{-7}	1.05×10^{-10}
5	1.06×10^{-7}	1.03×10^{-10}
6	1.04×10^{-7}	1.01×10^{-10}
7	0.702×10^{-7}	0.680×10^{-10}

Case 1 is the nominal case where the domain dimensions are as presented in Figure 3.2. For Cases 2, 3 and 4, tows in the same layer are moved together to mimic a uniform fiber layer displacement. Moving tows in the same layer together creates distinct flow channels between layers along the x-direction as shown in Figure 3.16 below. In Case 2, the same flow conditions are applied to a domain where tows #4 and #5 are moved 20 μm, and tows #6,# 7 and #8 are moved 40 μm in the positive y-direction, widening the 3rd main channel between the third and fourth tow layer by 40 μm. Similarly in Case 3, tows #4 and #5 are shifted $20\mu m$ in the positive y-direction while tows #6, #7 and #8 are shifted $20\mu m$ in the negative y-direction, thus widening the 2nd main channel between the second and third tow layer by $40\mu m$. Lastly, in Case 4, tows #4 and #5 are moved $40\mu m$, and tows #6, #7 and #8 are moved $20\mu m$ in the negative y-direction, widening the 1st main channel between the first and second tow layer by $40\mu m$.

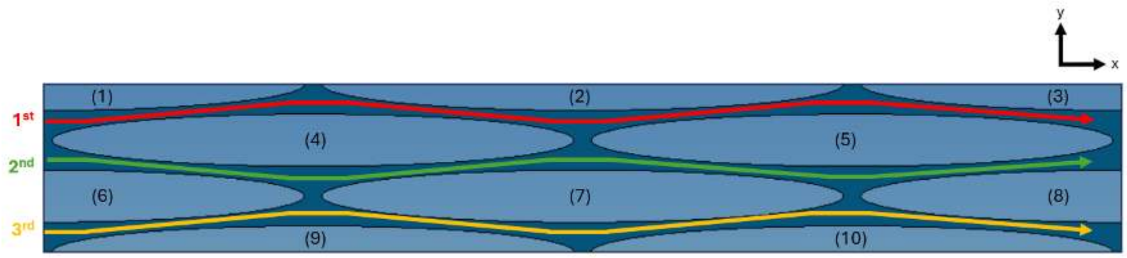

Figure 3.16: Three main channels between tow layers

In addition to the main channels, the domain geometry contains twelve horizontal channels between tows, as depicted in Figure 3.17. Each channel begins at the midpoint between two adjacent tows. For example, channel #6 starts at the midpoint between tows #6 and #7 and ends at the midpoint between tows #4 and #5. Cases 2, 3, and 4 represent dominant flow scenarios in channels #9-12, #5-8 and #1-4, respectively. Compared to the nominal Case 1, the overall permeability increases when the resin flow predominantly occurs in the channels created between the tow layers. This increase is expected since inter-tow flow channels provide less resistance to resin flow compared to the porous tow structure. Therefore, resin can flow more freely between inter-tow channels. It is noticeable that the overall permeability values of Cases 2, 3 and 4 are the same because the extreme geometries created by widening the channels in the same layer result in similar flow conditions

In Cases 5, 6, and 7, different flow channel formations are created by relocating the tows individually. When the tows in the same layer are moved independently, the observed overall permeability is higher than the nominal case; however, the permeability value is lower than the most extreme cases which are Case 2, 3 and 4.

In Case 7, it is observed that as the dominant flow channel develops more branches, the overall permeability value decreases due to the resin encountering greater resistance along a longer channel path.

The overall permeability results of the six extreme cases are compared with minimum, maximum and average channel gap (h) values of the dominant channels, as shown in Table 3.5. For each case, only the gaps of the dominant channels are considered, as the flow can be considered as negligible in the remaining non-dominant channels. There are twelve channels in the domain through which resin can choose to flow, as shown in Figure 3.17. For example, in Case 7, the flow is dominant on channels #1, #2, #6, #7, #9, and #12 whereas there is negligible resin flow in channels #3, #4, #5, #8, #10, and #11, as represented in Figure 3.18. Therefore, only the gaps between tows in the dominant channels are considered in the calculation of minimum, maximum, and average channel gaps.

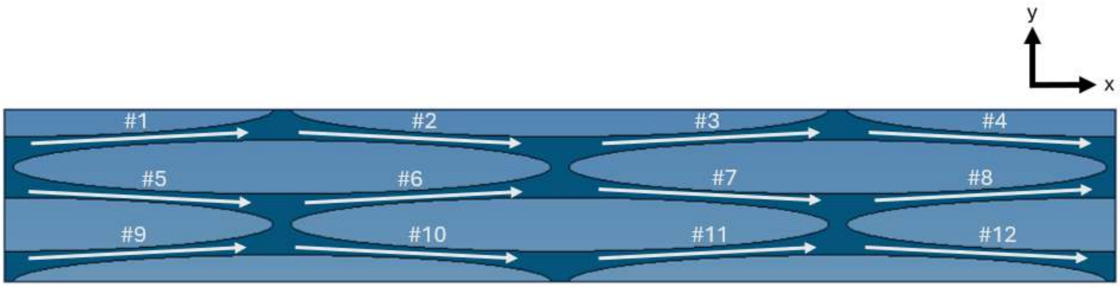

Figure 3.17: Possible horizontal channels between tows for resin flow

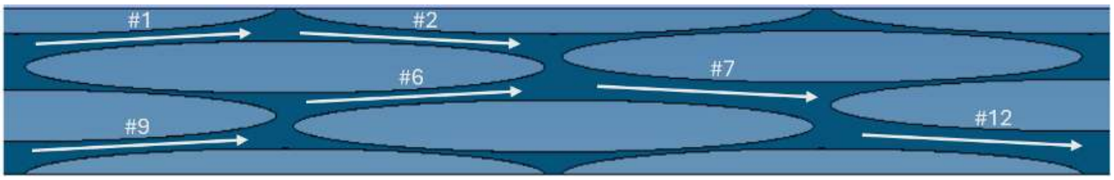

Figure 3.18: Dominant horizontal channels for Case 7

Table 3.5: Minimum, maximum and average channel gaps for the nominal and six extreme cases

Case	h_{min} $[\mu m]$	h_{max} $[\mu m]$	h_{avg} $[\mu m]$	K_o $[m^2]$
1	31.6	85.0	46.0	0.386×10^{-10}
2	71.6	125	86.0	1.05×10^{-10}
3	71.6	125	86.0	1.05×10^{-10}
4	71.6	125	86.0	1.05×10^{-10}
5	71.6	125	86.0	1.03×10^{-10}
6	71.6	125	86.0	1.01×10^{-10}
7	41.6	125	66.0	0.680×10^{-10}

Figure 3.19 shows the plot between overall permeability values and the minimum, maximum, and average channel gap values. A correlation is observed between the minimum and average channel gaps with overall permeability. However, the maximum channel gap does not exhibit a direct relation. For instance, in Case 7, the maximum channel gap is the same with other cases; however, the dominant channels are not identical to each other, which causes the minimum and average gap to be different.

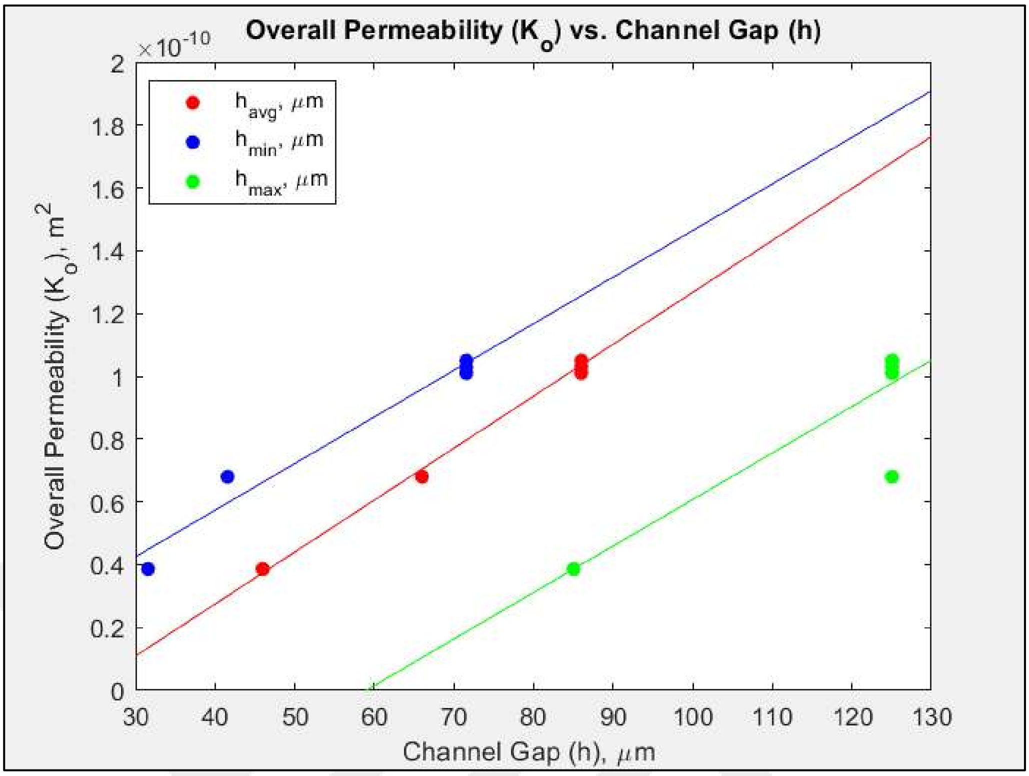

Figure 3.19: Overall permeability versus channel gaps for nominal and six extreme cases

3.7 *Gradual Variation of Channel Gaps*

In order to establish a correlation between overall permeability and the channel gap of the dominant flow channels, a gradual variation is applied to channel gaps in Case 2. Channel gaps h_9, h_{10}, h_{11} and h_{12} are gradually varied by adjusting the tow positions of tows #6, #7 and #8 as shown in Table 3.6.

Table 3.6: Tow center variation for gradually varying channel gaps in μm

Cases	Tow 1	Tow 2	Tow 3	Tow 4	Tow 5	Tow 6	Tow 7	Tow 8	Tow 9	Tow 10
1	(0,0)	(0,0)	(0,0)	(0,0)	(0,0)	(0,0)	(0,0)	(0,0)	(0,0)	(0,0)
2	(0,0)	(0,0)	(0,0)	(0,+20)	(0,+20)	(0,+40)	(0,+40)	(0,+40)	(0,0)	(0,0)
2.1	(0,0)	(0,0)	(0,0)	(0,+20)	(0,+20)	(0,+35)	(0,+35)	(0,+35)	(0,0)	(0,0)
2.2	(0,0)	(0,0)	(0,0)	(0,+20)	(0,+20)	(0,+30)	(0,+30)	(0,+30)	(0,0)	(0,0)
2.3	(0,0)	(0,0)	(0,0)	(0,+20)	(0,+20)	(0,+25)	(0,+25)	(0,+25)	(0,0)	(0,0)
2.4	(0,0)	(0,0)	(0,0)	(0,+20)	(0,+20)	(0,+20)	(0,+20)	(0,+20)	(0,0)	(0,0)
2.5	(0,0)	(0,0)	(0,0)	(0,+20)	(0,+20)	(0,+15)	(0,+15)	(0,+15)	(0,0)	(0,0)
2.6	(0,0)	(0,0)	(0,0)	(0,+20)	(0,+20)	(0,+10)	(0,+10)	(0,+10)	(0,0)	(0,0)

The resulting overall permeabilities from the simulations, along with the average, maximum, and minimum channel gaps for the dominant channels are presented in Table 3.7.

Table 3.7: Overall permeabilities and channel gaps for dominant channels for gradual variation of channel gaps

Cases	$K_{o,sim}$ [m^2]	h_{min} [μm]	h_{max} [μm]	h_{avg} [μm]
2	1.05×10^{-10}	71.6	125	86.0
2.1	0.882×10^{-10}	66.6	120	81.0
2.2	0.745×10^{-10}	61.6	115	76.0
2.3	0.638×10^{-10}	56.6	110	71.0
2.4	0.561×10^{-10}	51.6	105	66.0
2.5	0.515×10^{-10}	46.6	100	61.0
2.6	0.500×10^{-10}	41.6	95.0	56.0

The overall permeabilities are plotted against the average, maximum, and minimum channel gaps in Figure 3.20.

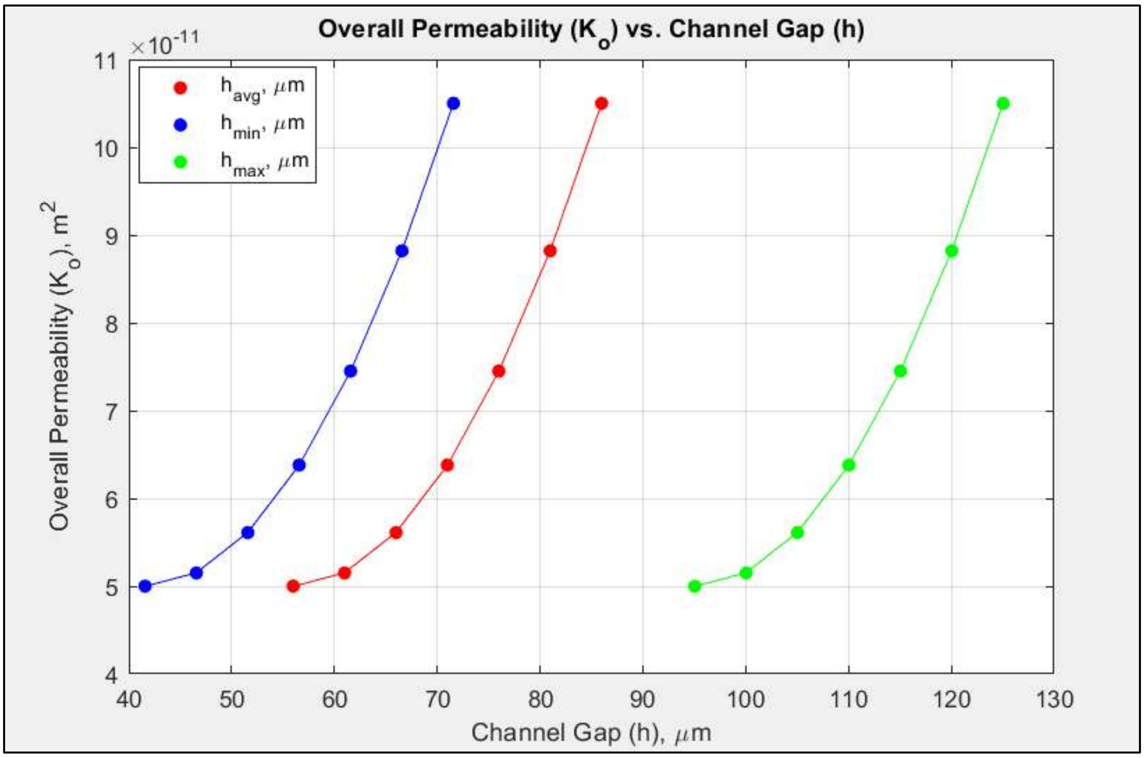

Figure 3.20: Overall permeability versus channel gap for gradually increasing channel gaps

Second-order polynomials are fitted to correlate the channel gaps to overall permeabilities, as described in Equation (3.16), (3.17), and (3.18) for minimum, average and maximum channel gaps, respectively.

$$K_o(h_{min}) = (0.0610)h_{min}^2 - (5.06 \times 10^{-6})h_{min} + (1.55 \times 10^{-10}) \quad (3.16)$$

$$K_o(h_{avg}) = (0.0610)h_{avg}^2 - (6.82 \times 10^{-6})h_{avg} + (2.41 \times 10^{-10}) \quad (3.17)$$

$$K_o(h_{max}) = (0.0610)h_{max}^2 - (1.16 \times 10^{-5})h_{max} + (6.00 \times 10^{-10}) \quad (3.18)$$

The overall permeability can be determined from the known dominant channel gaps by using Equations (3.16), (3.17), and (3.18).

3.8 Random Cases

Three randomly distributed flow cases are created in ANSYS Fluent. The tow center positions are assigned randomly using a MATLAB code. Similar to the extreme cases, the tows remain stationary along the x-axis, while only tows #4–8 are shifted along the y-axis, assuming tows #1–3 and #9–10 remain fixed. The variation of the tow centers from the nominal configuration for three random cases is provided in Table 3.8.

Table 3.8: Tow center variation for three random cases in μm

Cases	Tow 1	Tow 2	Tow 3	Tow 4	Tow 5	Tow 6	Tow 7	Tow 8	Tow 9	Tow 10
8	(0,0)	(0,0)	(0,0)	(0,+11.9)	(0,+0.8)	(0,+6.9)	(0,-11.1)	(0,-11.6)	(0,0)	(0,0)
9	(0,0)	(0,0)	(0,0)	(0,+18.6)	(0,-5.2)	(0,+18.9)	(0,+4.4)	(0,+11.3)	(0,0)	(0,0)
10	(0,0)	(0,0)	(0,0)	(0,+16.1)	(0,-0.4)	(0,+3.8)	(0,-9.6)	(0,+0.7)	(0,0)	(0,0)

The velocity distributions for each case are shown in Figure 3.21. Volumetric flow rate and overall permeability values computed from ANSYS simulation results are tabulated in Table 3.9.

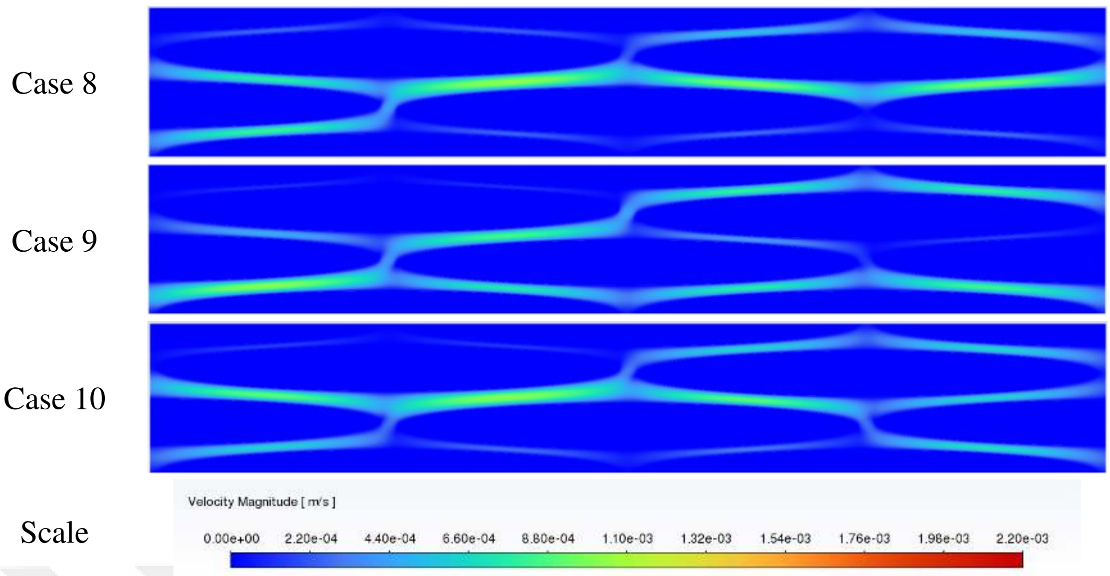

Figure 3.21: Velocity distribution graphs for three random cases

Table 3.9: Volumetric flowrate and overall permeability results of three random cases

Case	**Calculated Volumetric Flowrate from ANSYS** $Q_{inlet}\ [m^3/s]$	**Calculated Overall Permeability from** Q_{inlet} $K_o[m^2]$
8	4.90×10^{-8}	4.75×10^{-11}
9	4.98×10^{-8}	4.82×10^{-11}
10	4.81×10^{-8}	4.66×10^{-11}

3.9 Cases with Different Domain Size

Three additional cases are created by doubling the domain size along the x-axis, y-axis and both axes, respectively. The domain geometries are shown in Figure 3.22. The velocity distributions are shown in Figure 3.23. The volumetric flow rates and overall permeability results are presented in Table 3.10. The simulation results are the same for Cases 11, 12, and 13 since the tow distribution remains unchanged across all scenarios. Even though the domain size increases in different dimensions, the tow positions, as well as the intra-tow, inter-tow, and overall porosities, remain the same. Consequently, the overall permeabilities computed in ANSYS yield the same values for all three cases, as expected.

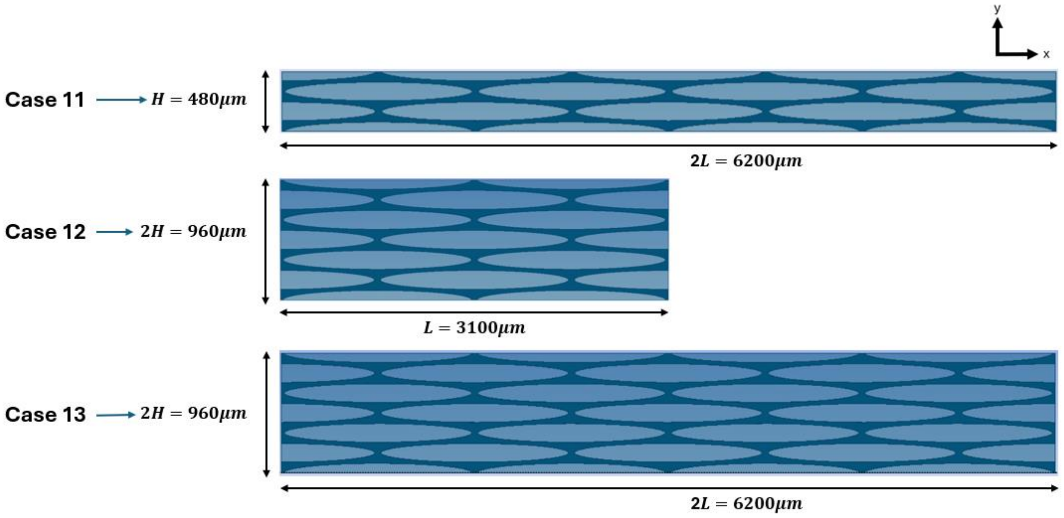

Figure 3.22: Domain geometries for Cases 11-13

Case 11

Case 12

Case 13

Scale

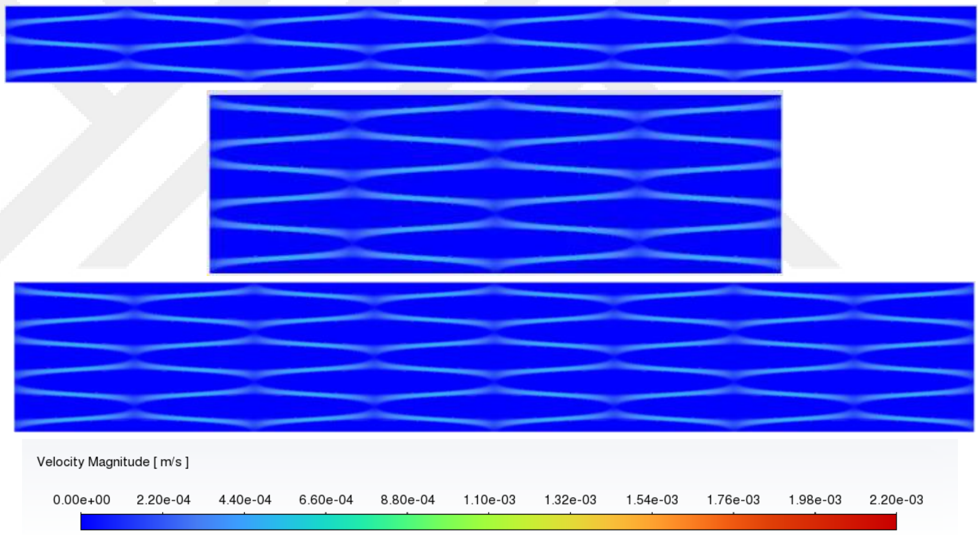

Figure 3.23: Velocity distribution graphs for Cases 11-13

Table 3.10: Volumetric flowrate and overall permeability for Cases 11-13

Case	Calculated Volumetric Flowrate from ANSYS Q_{inlet} $[m^3/s]$	Calculated Overall Permeability from Q_{inlet} $K_o[m^2]$
11	3.99×10^{-8}	3.86×10^{-11}
12	3.99×10^{-8}	3.86×10^{-11}
13	3.99×10^{-8}	3.86×10^{-11}

Chapter 4:
PERMEABILITY APPROXIMATION BY ELECTRIC-HYDRAULIC ANALOGY

Permeability is calculated by using the results of ANSYS Fluent simulation and Darcy's Law in Chapter 3. In this chapter, a permeability approximation method is developed from the Darcy's Law and Ohm's Law, which can achieve a degree of simplification in permeability characterization, lead to a better understanding of the dominant porous channels, and help determine the overall permeability of a preform with fibrous tows.

4.1 Assumptions and Formulation

It can be observed from the ANSYS Fluent simulation velocity contours that resin primarily flows through the inter-tow channels marked in Figure 3.16. As the resin flows into the tows under the driving force of the pressure gradient between the inlet and the outlet, most of it is expected to flow through the inter-tow channels formed by the spaces between the elliptic tows. These channels offer significantly less resistance to flow compared to the porous tows, making them the primary pathways for resin movement.

A defining characteristic of these channels is the channel gap (h) in the vertical direction, which varies along the horizontal direction due to the elliptical shape of the tows. Figure 4.1 illustrates the channel gap h, where h is measured in the y-direction and varies along the x-direction.

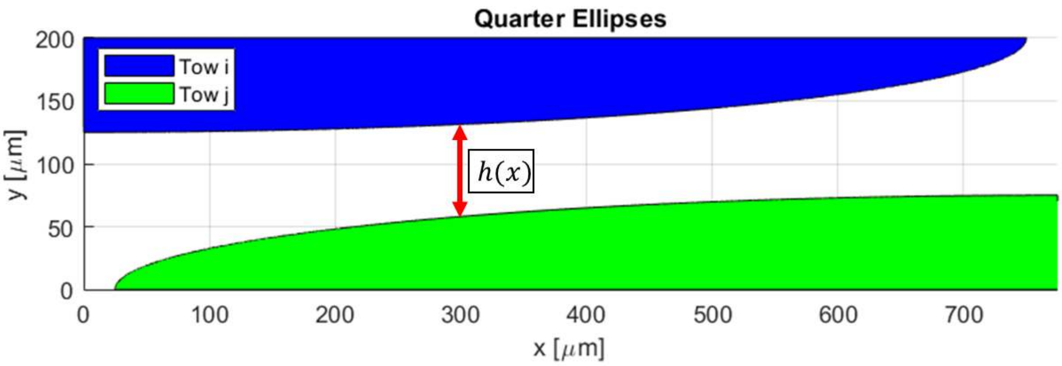

Figure 4.1: Unit cell of a channel and channel gap "h"

For the electric-hydraulic analogy, there are two key assumptions to be made: negligible intra-tow resin flow and channel thickness dominance. Prior to that, it is important to note that as resins used in composite materials manufacturing processes are highly viscous and they flow in the fiber preform with very low Reynold's numbers, Stokes flow is valid for resin flow [19].

Firstly, since the permeability of the tows is significantly lower than that of the inter-tow regions, it can be assumed that the resin flow in the intra-tow region is negligible. Thus, the permeability and the porosity of the tows are disregarded, and the tows are treated as solid objects. It is worth noting that this assumption is commonly made in literature for similar cases as well [20].

Secondly, the channel thickness, Z, is assumed to be much larger than channel gap (Z≫h). Since the simulated ANSYS model is two-dimensional, the domain thickness is set to 1 m by default, which is considerably larger than the channel gaps measured in the micrometer scale. This satisfies the conditions for channel gap-to-thickness ratio of Stokes flow permeability in a thin rectangular channel. It is also assumed that the channel gaps between adjacent tows are constant and rectangular. As the channel gap is changing throughout the channel, the selection of channel gap value will be further discussed in Section 4.2.

Due to the multiple channels included in this case, a relation must be derived between the permeability of the overall domain and the individual channels. First step is to rewrite the Darcy's Law from Equation (1.1). As the length scale is constant between the beginning and the end of the channels, which is L, Darcy's Law can also be expressed as in Equation (4.1), where the pressure gradient in Equation (1.1) is represented discretely in terms of Δp, which is the pressure difference between the inlet and the outlet, and L, which is the distance between the inlet and the outlet.

$$Q = \frac{KA}{\mu L} \Delta p \tag{4.1}$$

Darcy's Law, as shown in Equation (4.1), is used to express flow of a fluid in a porous domain. Darcy's Law similarity to Ohm's Law, used in electrical circuits, shown in Equation (4.2), is used for permeability approximation. In an electrical circuit, current decreases as resistance increases under a constant voltage. Similarly, Darcy's Law relates resin flow rate to the pressure difference, which corresponds to voltage in Ohm's Law. In this analogy, the resin flow rate represents the electrical current, and the resistance is represented by a constant defined as the product of viscosity and channel length divided by the product of permeability and cross-sectional area. Table 4.1 outlines the parameter correspondence the electric-hydraulic analogy between Darcy's Law and Ohm's Law. [21]

$$I = \frac{1}{R}V \tag{4.2}$$

Table 4.1: Analogy between the parameters of Darcy's Law and Ohm's Law

Darcy's Law	**Ohm's Law**
Q	I
$\frac{\mu L}{KA}$	R
Δp	V

Q is volumetric flowrate of resin in m^3/s, I is electric current in $Ampere$, μ is viscosity of resin in $Pa.s$, L is domain length in m, K is permeability in m^2, A is cross-sectional area in m^2, R is electric resistance in Ω, Δp is pressure difference in Pa, V is voltage in V.

In this analogy, hydraulic resistance R_{hyd} can be expressed as in Equation (4.3), where it is analogous to the electric resistance R in Equation (4.2). Then, the hydraulic Equation (4.4) is analogous to the electric Equation (4.2).

$$R_{hyd} = \frac{\mu L}{kA} \tag{4.3}$$

$$Q = \frac{1}{R_{hyd}}\Delta p \tag{4.4}$$

4.2 Permeability Approximation for Tow Layer Displacement

In the first three extreme cases, three main channels are identified as the primary pathways for resin flow as shown in Figure 3.16. Let R_{eff} represent the overall hydraulic resistance of the complete domain, and R_n denote the hydraulic resistance of the n^th^

channel in Figure 3.16. Using the electric-hydraulic analogy, each channel can be considered analogous to a resistor. Therefore, these channels can be represented as three resistors connected in parallel as illustrated in Figure 4.2.

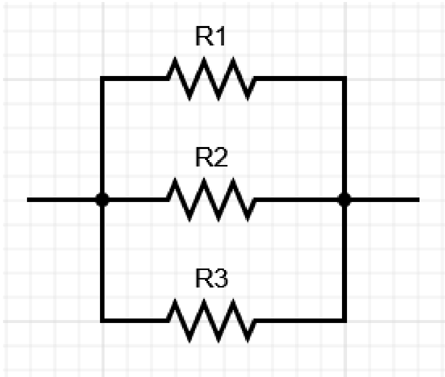

Figure 4.2: Three resistors in parallel, representing main flow channels in tow domain

Following the principles of parallel resistance, the hydraulic resistance for the set of three parallel channels is expressed as in Equation (4.5).

$$\frac{1}{R_{eff}} = \sum_{n=1}^{3} \frac{1}{R_n} = \frac{1}{R_1} + \frac{1}{R_2} + \frac{1}{R_3} \tag{4.5}$$

Substituting Equation (4.3) into each term of Equation (4.5), with respect to the individual channels and the overall domain, results in Equation (4.6).

$$\frac{k_{eff}A_{eff}}{\mu L} = \frac{k_1 A_1}{\mu L} + \frac{k_2 A_2}{\mu L} + \frac{k_3 A_3}{\mu L} \tag{4.6}$$

As this study is conducted in two-dimensions, area is defined as the channel gap multiplied by the unit depth. Simplifying Equation (4.6) in terms of effective and channel permeabilities results in Equation (4.7).

$$k_{eff}H = k_1 h_1 + k_2 h_2 + k_3 h_3 \tag{4.7}$$

Next, the Stokes flow assumption is introduced. The permeability of a thin channel with a rectangular cross section in Stokes flow is given by Equation (4.8) [1], which is assumed to hold for the inter-tow channels in this case.

$$k_{Stokes} = \frac{1}{12} {h_n}^2 = k_n \tag{4.8}$$

Substituting Equation (4.8) into the channel terms of Equation (4.7) yields in Equation (4.9).

$$k_{eff}H = \frac{{h_1}^3}{12} + \frac{{h_2}^3}{12} + \frac{{h_3}^3}{12} \tag{4.9}$$

Rearranging Equation (4.9) provides a simple equation for the overall permeability in terms of the channel gaps and the domain gap, as shown in Equation (4.10).

$$k_{eff} = \frac{{h_1}^3 + {h_2}^3 + {h_3}^3}{12H} \tag{4.10}$$

Further simplifications can be applied for special cases. For nominal Case 1, where the tows are uniformly distributed, h_1, h_2 and h_3 are equal as defined in Equation (4.11).

$$h_1 = h_2 = h_3 \equiv h \tag{4.11}$$

Substituting h from Equation (4.11) into Equation (4.10) results in the specific equation of overall permeability for Case 1, as shown in Equation (4.12).

$$k_{eff} = \frac{h^3}{4H} \tag{4.12}$$

Extreme Cases 2, 3 and 4 represent scenarios where one of the main channels is significantly expanded, causing the other channels to narrow down to the extent that minimal or no resin flow is observed in them. This imitates a tow layer displacement. In these cases, the channel through, which most of the resin flow occurs, is referred to as the dominant channel, while the other channels are referred as non-dominant channels.

Channel gap statistics for four cases are presented in Table 4.2. The channel gap values for the non-dominant channels are smaller as expected. As a result, the cube of the channel gap value for non-dominant channels will be much smaller than the channel gap value used for the dominant channel. Consequently, the contribution of the non-dominant channels to the approximate overall permeability is negligible. Therefore, the channel gap terms for the non-dominant channels can be omitted from the general permeability approximation calculations in Equation (4.10).

Thus, for Cases 2, 3, and 4, Equation (4.10) is simplified as shown in Equations (4.13), (4.14) and (4.15).

Case 2 (Dominant channel is 3rd main channel in Figure 3.16):

$$h_3 \gg h_1 \;\&\; h_3 \gg h_2 \;\rightarrow\; k_{eff} = \frac{{h_3}^3}{12H} \tag{4.13}$$

Case 3 (Dominant channel is 2nd main channel in Figure 3.16):

$$h_2 \gg h_1 \;\&\; h_2 \gg h_3 \;\rightarrow\; k_{eff} = \frac{{h_2}^3}{12H} \tag{4.14}$$

Case 4 (Dominant channel is 1st main channel in Figure 3.16):

$$h_1 \gg h_2 \;\&\; h_1 \gg h_3 \;\rightarrow\; k_{eff} = \frac{{h_1}^3}{12H} \tag{4.15}$$

In order to validate the derived approximation equations (Equations (4.12-15)), their results will be compared to those obtained using the conventional method of calculating the permeability of a flow domain. The validity of neglecting the non-dominant channels in the permeability approximation for Cases 2, 3 and 4 will also be evaluated by comparing results derived from using case-specific Equations (4.13), (4.14) and (4.15) with those obtained using the general case equation in Equation (4.10) without neglecting any channel.

Channel gap statistics for each case are presented in Table 4.2, and a sample of the channel gap throughout a channel in Case 1 is given in Figure 4.3. Due to the elliptical nature of the channel boundaries, it is observed from Figure 4.3 and Table 4.1 that the channel gap values are more frequently grouped near the minimum channel gap rather than the maximum channel gap. As a result, the statistical significance of the maximum channel gap is lower compared to the average and minimum channel gaps. Therefore, this study excludes the maximum channel gap values from further analysis.

Table 4.2: Channel gap statistics for Cases 1-4

	Case 1	**Cases 2, 3 and 4**	**Cases 2, 3 and 4**
	All Channels	**Dominant Channel**	**Non-Dominant Channels**
$\boldsymbol{h_{min}}$ **[m]**	3.16×10^{-5}	7.16×10^{-5}	1.16×10^{-5}
$\boldsymbol{h_{max}}$ **[m]**	8.50×10^{-5}	12.5×10^{-5}	6.50×10^{-5}
$\boldsymbol{h_{avg}}$ **[m]**	4.60×10^{-5}	8.60×10^{-5}	2.60×10^{-5}
Standard Deviation [m]	1.55×10^{-5}	1.55×10^{-5}	1.55×10^{-5}

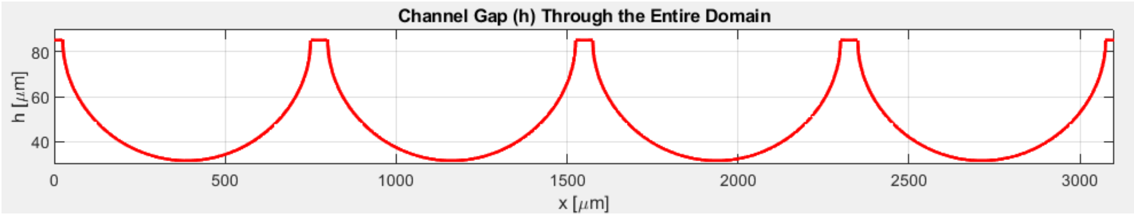

Figure 4.3: Channel gap variation along the domain length for Case 1

The overall permeability of the domain is first calculated using ANSYS Fluent simulation results and Darcy's Law. The results are referred to as the simulated overall permeability ($K_{o,sim}$). Table 4.3 shows the overall permeability values using the case-specific approximation equations (Equations (4.9-12)), referred to as the approximated overall permeability ($K_{o,app}$).

The Stokes flow assumption used in derivation of these equations is that the channel gap remains constant throughout the channel. However, due to the elliptical structure of the channel boundaries, channel gap varies along x-direction, as can be seen in Figure 4.3. To account for this variability, six different statistical values of the channel gap, listed in the first column of Table 4.3, are evaluated to identify which value serves as the most reliable reference for permeability approximation. STD stands for standard deviation.

Table 4.3: Approximated overall permeabilities for Cases 1-4 calculated by using different reference channel gaps

Reference Channel Gap	**Case 1 Approximated Permeability $K_{o,app}$ [m²]**	**Case 2, 3, and 4 Approximated Permeability $K_{o,app}$ [m²]**
$h_{min} - 1STD$	0.215×10^{-11}	3.06×10^{-11}
h_{min}	1.64×10^{-11}	6.37×10^{-11}
$h_{min} + 1STD$	5.44×10^{-11}	11.6×10^{-11}
$h_{avg} - 1STD$	1.47×10^{-11}	6.07×10^{-11}
h_{avg}	5.07×10^{-11}	11.0×10^{-11}
$h_{avg} + 1STD$	12.1×10^{-11}	18.2×10^{-11}

Table 4.4 presents the permeability ratios of the approximated permeability to the simulated permeability for each reference channel gap used in the calculation.

Table 4.4: Approximated and simulated permeability ratios for Cases 1-4

Reference Channel Gap	**Case 1 Permeability Ratio $K_{o,app}/K_{o,sim}$**	**Case 2, 3, and 4 Permeability Ratio $K_{o,app}/K_{o,sim}$**
$h_{min} - 1STD$	0.06	0.29
h_{min}	0.42	0.61
$h_{min} + 1STD$	1.41	1.10
$h_{avg} - 1STD$	0.38	0.58
h_{avg}	1.31	1.05
$h_{avg} + 1STD$	3.13	1.73

It is expected that the minimum channel gap to dominate the permeability of the channel and, by extension, the domain, as it represents a choke point constrained by tows with very low permeability. On the other hand, one might also intuitively expect the permeability to be mostly related to the average channel gap. From Table 4.4, permeability ratio calculated using the approximation equation with h_{avg} as the reference channel gap is the closest to 1, followed by the result using $h_{min} + 1STD$. This indicates that h_{avg} is the most suitable value for approximating the overall permeability.

An elaboration is necessary on the assumption of resin flow through non-dominant channels is negligibly small, which is used to derive Equations (4.13-15). This assumption simplifies Equation (4.10) by eliminating two variables, making the approximate permeability dependent on only one variable and thus easier to compute. However, this computational simplicity comes at the potential cost of reduced accuracy. To evaluate the accuracy trade-off, approximate permeabilities for Cases 2, 3 and 4 are recalculated using Equation (4.10) without assuming negligible flow in non-dominant channels. The results are presented in Table 4.5 and the permeability ratios are shown in Table 4.6.

Comparing both approaches reveals that there is negligible difference between the two permeabilities. It is expected that the approximate permeabilities found with Equation (4.10) would be closer to the simulated permeabilities than those found with Equations (4.13-15). However, in all cases except for the permeability approximated from h_{min}, the general approach yields to a higher error. This discrepancy may be caused by assumptions and limitations of the approximation method, which will be discussed in Chapter 5.

Table 4.5: Approximated permeabilities of Cases 2-4 using the general case equation

Reference Channel Gap	**Approximated Permeability $K_{o,app}$ [m^2]**
$h_{min} - 1STD$	3.06×10^{-11}
h_{min}	6.43×10^{-11}
$h_{min} + 1STD$	12.2×10^{-11}
$h_{avg} - 1STD$	6.12×10^{-11}
h_{avg}	11.7×10^{-11}
$h_{avg} + 1STD$	20.6×10^{-11}

Table 4.6: Permeability ratios of Cases 2-4 using the general case equation

Reference Channel Gap	**Permeability Ratio $K_{o,app}/K_{o,sim}$**
$h_{min} - 1STD$	0.29
h_{min}	0.61
$h_{min} + 1STD$	1.16
$h_{avg} - 1STD$	0.58
h_{avg}	1.11
$h_{avg} + 1STD$	1.96

4.3 *Standardization of Permeability Approximation*

To standardize the permeability approximation method for all extreme and random cases, the domain geometry shown in Figure 3.1 is assumed to act as an electric circuit where channel gaps between tows in both x- and y-directions act as resistors as illustrated in Figure 4.4. Flow domain is represented as a circuit including 15 resistors as in Figure 4.5.

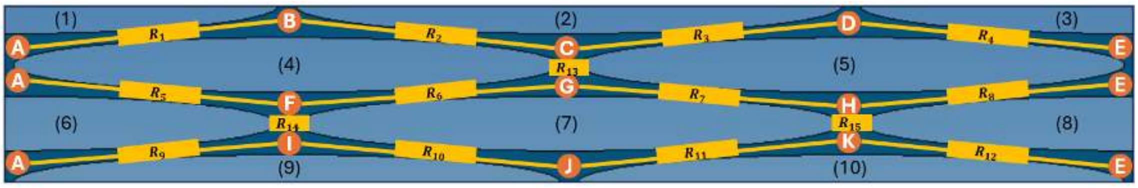

Figure 4.4: Electric-hydraulic analogy for the tow domain

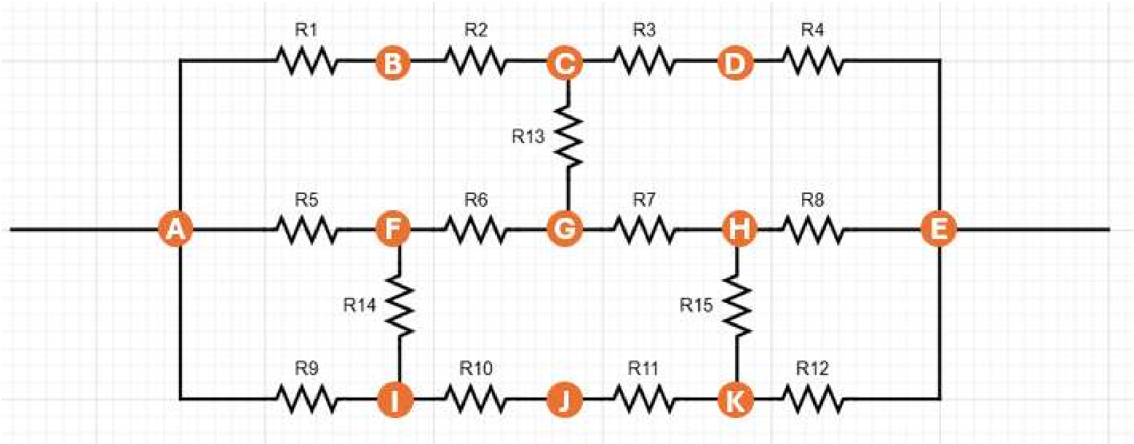

Figure 4.5: Representation of tow domain as an electric circuit

For overall permeability approximation, effective resistance between point A and E is computed. The calculation of the effective resistance is shown in Appendix D step by step. Effective resistance is expressed in Equation (4.16).

$$R_{eff} = R_i + \left(\left(\frac{1}{R_j + R_3 + R_4}\right) + \left(\frac{1}{R_p + R_b + R_m}\right)\right)^{-1} \tag{4.16}$$

The permeability of a thin channel with a rectangular cross section in Stokes flow is defined as in Equation (4.17).

$$K_{Stokes} = \frac{1}{12}h^2 \tag{4.17}$$

For each channel (for n=1:15) permeability is represented as in Equation (4.18).

$$K_n = \frac{1}{12}{h_n}^2 \tag{4.18}$$

Cross-sectional area is defined as channel gap times thickness in z direction as in Equation (4.19). Z is equal to 1 m since the domain is two dimensional.

$$A_n = h_n Z \tag{4.19}$$

For each channel, resistance can be written as in Equation (4.20).

$$R_n = \frac{\mu L_n}{k_n A_n} = \frac{12\mu L_n}{h_n^2 A_n} = \frac{12\mu L_n}{h_n^3 Z} = \frac{12\mu L_n}{h_n^3} \tag{4.20}$$

Effective resistance is calculated as explained in Appendix D from Equation (4.16). From Darcy's and Ohm's Law analogy in Equation (4.21), the effective permeability can be calculated as in Equation (4.22). A MATLAB code is written to calculate the effective permeability by calculating the effective resistance of the domain from resistance of each channel gap shown in Figure 4.4.

$$R_{eff} = \frac{\mu L}{K_{eff} A} \tag{4.21}$$

$$K_{eff} = \frac{\mu L}{R_{eff} A} \tag{4.22}$$

For standardization of the approximation, the channel gaps are defined for both horizontal and vertical channels in the domain. For horizontal channels #1-12, h is defined as distance between tows in y-direction. For vertical channels #13-15, h is defined as distance between tows in x-direction. As discussed in Section 4.2, the average channel gap, h_{avg}, will be used for the permeability approximation as it results in better agreement with the simulated permeabilities.

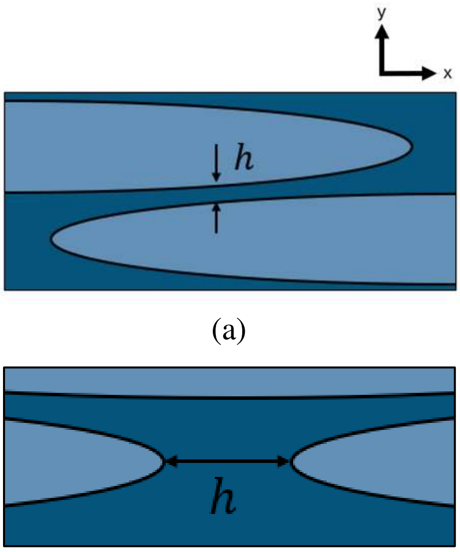

(b)

Figure 4.6: Channel gap (h) for (a) horizontal, and (b) vertical channels

The simulated overall permeabilities are compared with the approximated overall permeabilities from the electric-hydraulic circuit analogy as shown in Table 4.7. Simulated and approximated permeabilities show agreement with a maximum permeability ratio of 1.31. This validates the effectiveness of the electrical circuit analogy for permeability approximation.

Table 4.7: Simulated and approximated overall permeability comparison for 13 cases

Case	**Simulated Overall Permeability** $K_{o,sim}$ $[m^2]$	**Approximated Overall Permeability** $K_{o,app}$ $[m^2]$	**Permeability Ratio** $K_{o,app}/K_{o,sim}$
1	0.386×10^{-10}	0.508×10^{-10}	1.31
2	1.05×10^{-10}	1.17×10^{-10}	1.11
3	1.05×10^{-10}	1.17×10^{-10}	1.11
4	1.05×10^{-10}	1.17×10^{-10}	1.11
5	1.03×10^{-10}	1.16×10^{-10}	1.13
6	1.01×10^{-10}	1.16×10^{-10}	1.15
7	0.680×10^{-10}	0.820×10^{-10}	1.21
8	0.475×10^{-10}	0.598×10^{-10}	1.26
9	0.482×10^{-10}	0.608×10^{-10}	1.26
10	0.466×10^{-10}	0.593×10^{-10}	1.27
11	0.386×10^{-10}	0.508×10^{-10}	1.31
12	0.386×10^{-10}	0.508×10^{-10}	1.31
13	0.386×10^{-10}	0.508×10^{-10}	1.31

Additionally, the simulated permeability results of the gradual variation cases from Section 3.7 are compared with the results of permeability approximated by the electric analogy presented in Chapter 4. The results are matching with a maximum ratio of 1.28 between two permeabilities. It is observed that as the channel gap decreases, the percent error in the approximation increases. With a smaller channel gap, less resin flows through the inter-tow space, while more resin flows through the intra-tow space. Since this scenario conflicts with the approximation method's assumption of no intra-tow flow, the error becomes higher.

Table 4.8: Comparison of simulated and approximated permeabilities for gradually varying channel gap

Cases	**Simulated Overall Permeability $K_{o,sim}$ (m^2)**	**Approximated Overall Permeability $K_{o,app}$ (m^2)**	**Permeability Ratio $K_{o,app}/K_{o,sim}$**
2.0	1.05×10^{-10}	1.16×10^{-10}	1.11
2.1	0.882×10^{-10}	1.00×10^{-10}	1.14
2.2	0.745×10^{-10}	0.873×10^{-10}	1.17
2.3	0.638×10^{-10}	0.771×10^{-10}	1.21
2.4	0.561×10^{-10}	0.698×10^{-10}	1.24
2.5	0.515×10^{-10}	0.655×10^{-10}	1.27
2.6	0.500×10^{-10}	0.640×10^{-10}	1.28

Another comparison is made between the simulated permeability for domains with and without inlet and outlet pools, which is explained in Section 3.4. The percent error for the case without inlet and outlet pools is lower than that of the one with pools. The former case shows better agreement with the approximated permeabilities.

Table 4.9: Comparison of simulated and approximated permeabilities for cases with and without inlet and outlet pools

Reference Channel Gap	**Case 2 without inlet and outlet pools Permeability Ratio $K_{o,app}/K_{o,sim}$**	**Case 2 with inlet and outlet pools Permeability Ratio $K_{o,app}/K_{o,sim}$**
$h_{min} - 1STD$	0.29	0.19
h_{min}	0.61	0.39
$h_{min} + 1STD$	1.16	0.74
$h_{avg} - 1STD$	0.58	0.37
h_{avg}	1.11	0.71
$h_{avg} + 1STD$	1.96	1.26

Chapter 5:

LIMITATIONS OF PERMEABILITY APPROXIMATION

The limitations of permeability approximation using the electric-hydraulic analogy are studied by varying the intra-tow porosity and the domain height.

5.1 Effect of Varying Intra-tow Porosity

Simulations are conducted for varying intra-tow porosities of 40%, 50%, 60%, 70% and 80%. The approximated permeability remains constant for varying intra-tow porosity, as the approximation method assumes that there is no resin flow in the intra-tow regions. The approximated and simulated permeabilities for varying porosities are tabulated in Table 5.1 and permeability ratios are presented in Table 5.2. The overall permeabilities for each case are plotted against the varying intra-tow porosities in Figure 5.1.

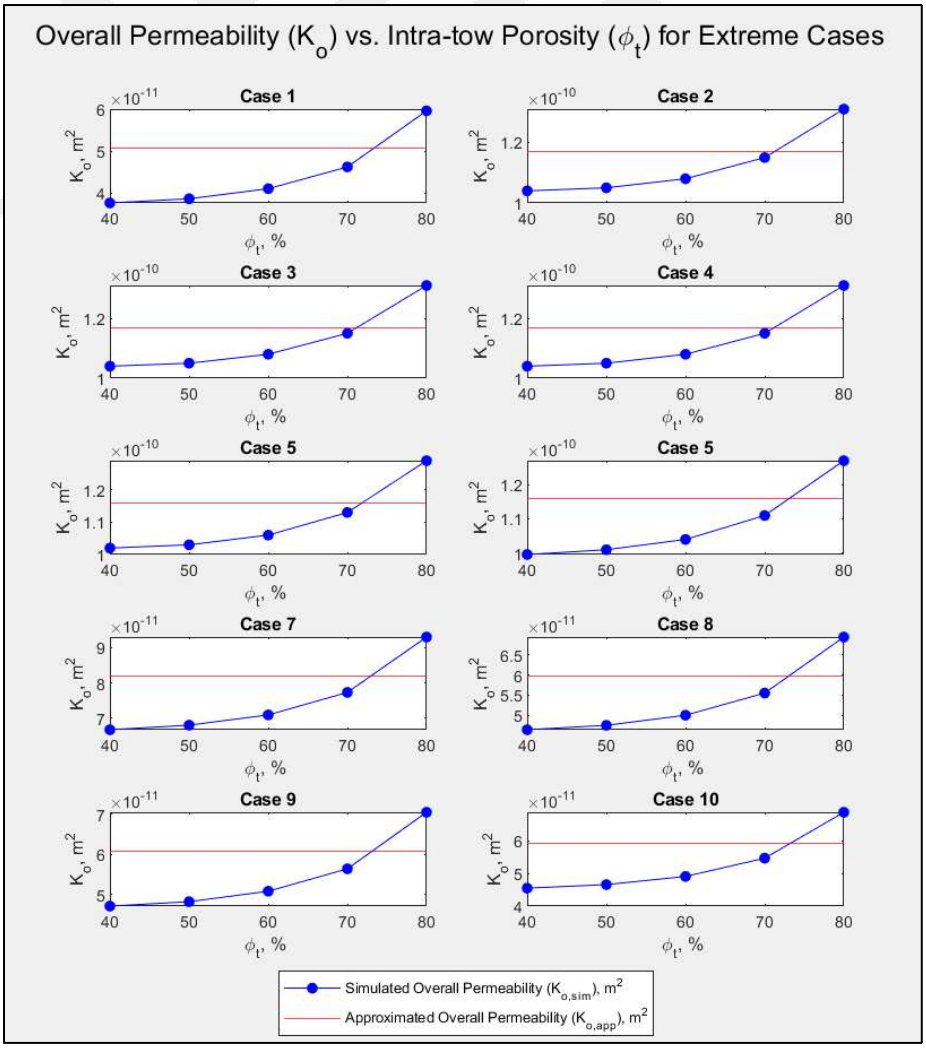

Figure 5.1: Change in overall permeability across varying intra-tow porosities

Table 5.1: Approximated and simulated permeabilities for varying intra-tow porosity of 13 cases

Case	$K_{o,app}$ $[m^2]$ $(\times 10^{-10})$	$K_{o,sim}$ $[m^2]$ $(\times 10^{-10})$				
		$\emptyset_t = 40\%$	$\emptyset_t = 50\%$	$\emptyset_t = 60\%$	$\emptyset_t = 70\%$	$\emptyset_t = 80\%$
1	0.508	0.376	0.386	0.410	0.462	0.596
2	1.17	1.04	1.05	1.08	1.15	1.31
3	1.17	1.04	1.05	1.08	1.15	1.31
4	1.17	1.04	1.05	1.08	1.15	1.31
5	1.16	1.02	1.03	1.06	1.13	1.29
6	1.16	0.996	1.01	1.04	1.11	1.27
7	0.820	0.667	0.680	0.709	0.773	0.930
8	0.598	0.464	0.475	0.500	0.555	0.694
9	0.608	0.471	0.482	0.508	0.564	0.705
10	0.593	0.455	0.466	0.491	0.547	0.688
11	0.508	0.376	0.386	0.410	0.462	0.596
12	0.508	0.376	0.386	0.410	0.462	0.596
13	0.508	0.376	0.386	0.410	0.462	0.596

As expected, the overall permeability increases with increasing intra-tow porosity. This occurs because as intra-tow porosity increases, more resin flows through the intra-tow regions. The amount of increasing resin flow in the intra-tow regions results in a higher overall permeability of the domain.

The approximated permeability remains unaffected from the variation in intra-tow porosity since the permeability approximation neglects intra-tow flow. Despite this limitation, the approximated permeability closely matches the simulated results when intra-tow porosity is near 70%, showing the minimum ratio between approximated and simulated permeabilities for this porosity value. Even though there is no relation between the intra-tow porosity and the approximated porosities, the results seem to show a close approximation when the intra-tow porosity is 70%.

Table 5.2: Comparison of approximated and simulated permeabilities for varying intra-tow porosity of 13 cases

Case	$K_{o,app}/K_{o,sim}$				
	$\emptyset_t = 40\%$	$\emptyset_t = 50\%$	$\emptyset_t = 60\%$	$\emptyset_t = 70\%$	$\emptyset_t = 80\%$
1	1.35	1.31	1.24	1.10	0.85
2	1.13	1.11	1.08	1.02	0.89
3	1.13	1.11	1.08	1.02	0.89
4	1.13	1.11	1.08	1.02	0.89
5	1.15	1.13	1.10	1.03	0.90
6	1.17	1.15	1.12	1.05	0.91
7	1.23	1.21	1.16	1.06	0.88
8	1.29	1.26	1.20	1.08	0.86
9	1.29	1.26	1.20	1.08	0.86
10	1.30	1.27	1.20	1.08	0.86
11	1.35	1.31	1.24	1.10	0.85
12	1.35	1.31	1.24	1.10	0.85
13	1.35	1.31	1.24	1.10	0.85

The velocity vectors for the uniform tow distribution with intra-tow porosities of 50% and 80% are shown in Figure 5.2 and 5.3. The velocity vectors are predominantly oriented around the porous tow regions with almost no visible flow within the intra-tow regions. When comparing the velocity vectors for intra-tow porosities of 50% and 80%, the velocity vectors are more prominent in the 80% intra-tow porosity case, as higher porosity allows more resin to flow through the tows.

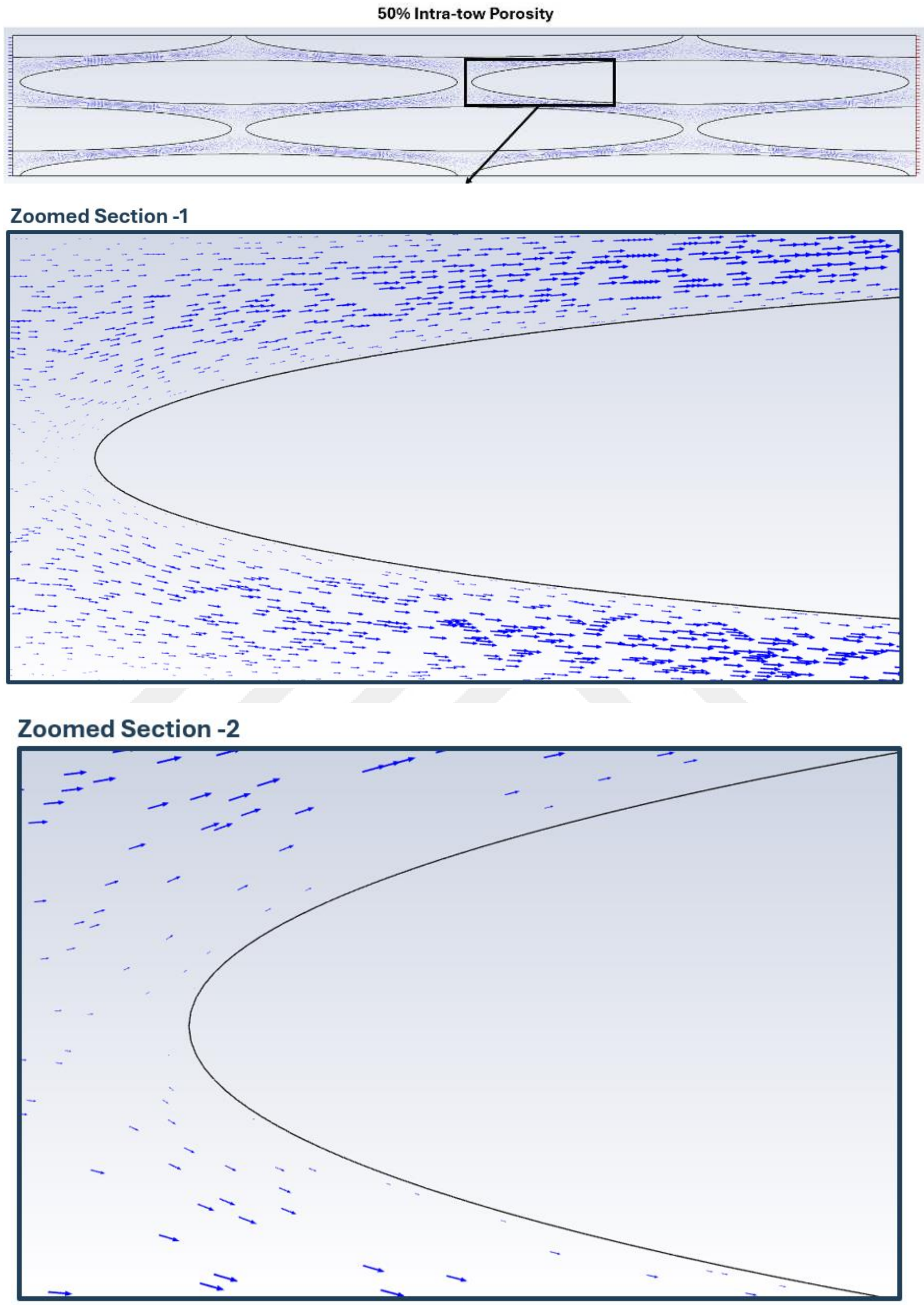

Figure 5.2: Velocity vectors for 50% intra-tow porosity

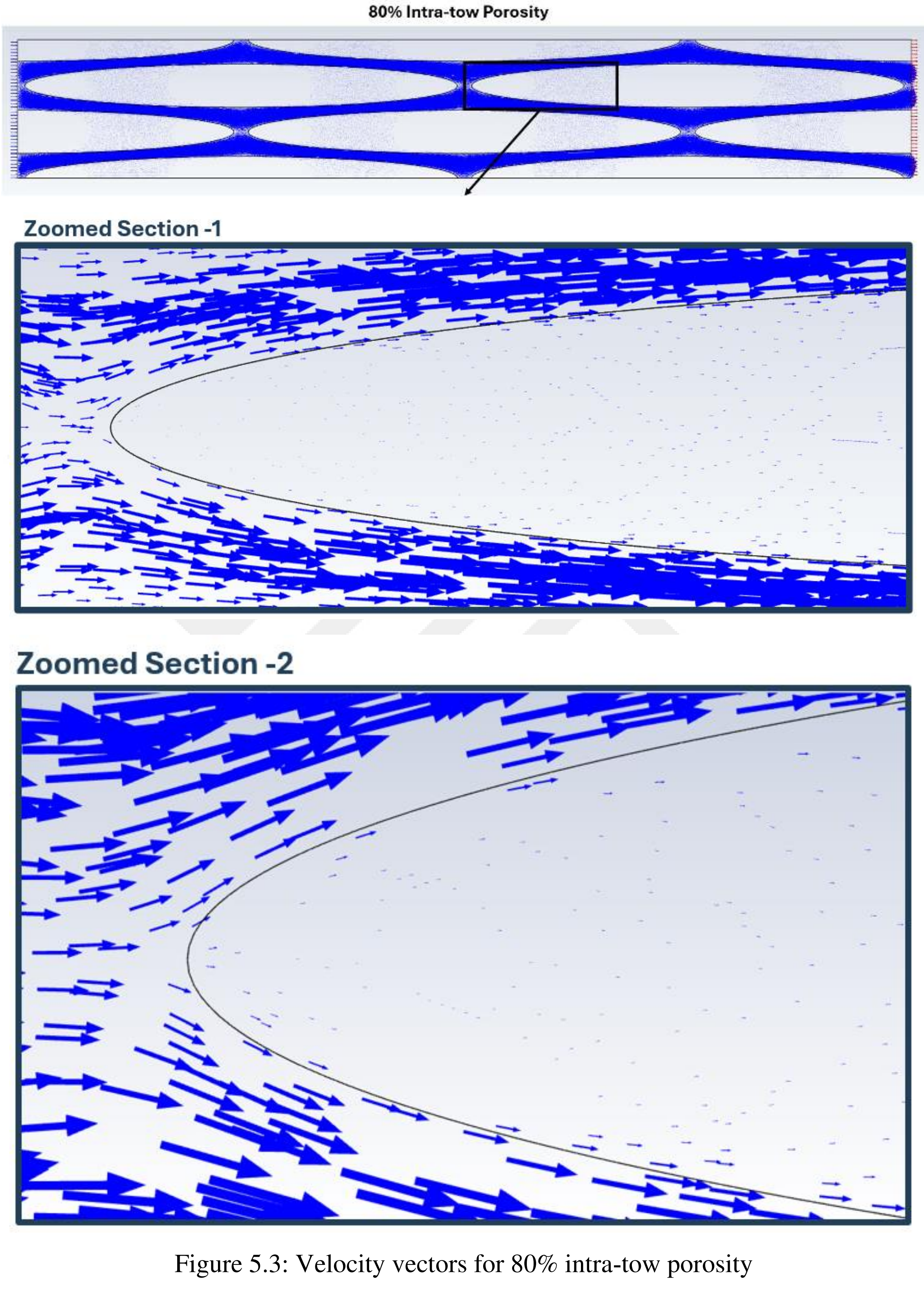

Figure 5.3: Velocity vectors for 80% intra-tow porosity

5.2 *Effect of Varying Domain Height*

Another limitation in the overall permeability approximation arises from variation in domain height, which affects the flow in the inter-tow and intra-tow regions. The extreme cases are simulated for narrower and wider domains while maintaining a constant intra-tow porosity. However, the global porosity changes since the domain size is adjusted by keeping tow size the same.

At first, the domain height is decreased to $H = 450\mu m$ as shown in Figure 5.4. Since intra-tow porosity is kept constant at 50%, the inter-tow porosity becomes 24% and the overall porosity becomes 62%. The simulated and approximated overall permeabilities are tabulated in Table 5.3. As domain height decreases, the channel gaps between the tows also decreases, leading to reduced overall permeability as expected. However, the approximated and simulated permeabilities show significant discrepancies, reflecting a limitation of the approximation method in narrower domains.

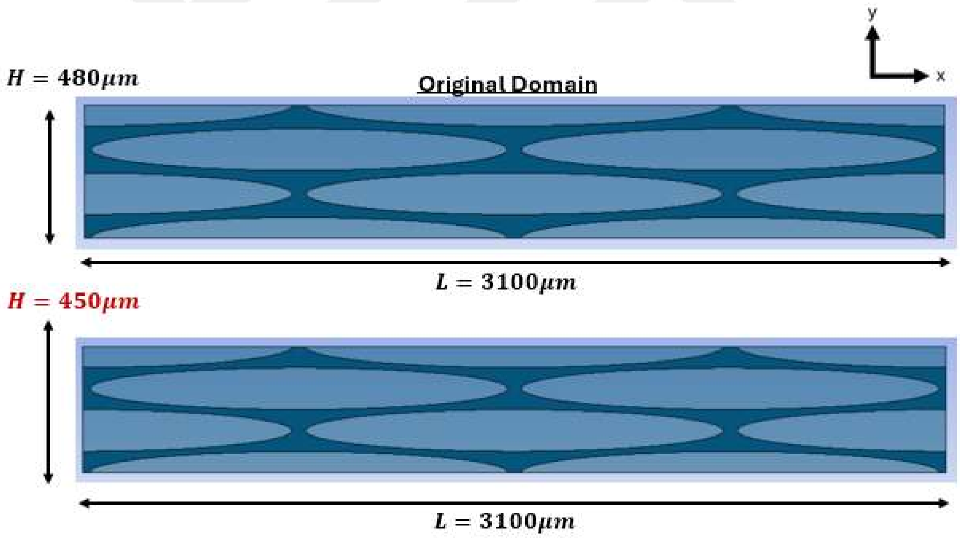

Figure 5.4: Tow domain for domain height $H = 450\ \mu m$

Table 5.3: Simulated and approximated permeabilities for domain height $H = 450\ \mu m$

Case	$K_{o,sim}\ [m^2]$ $(\times 10^{-10})$	$K_{o,app}\ [m^2]$ $(\times 10^{-10})$	$K_{o,app}/K_{o,sim}$
1	0.158	0.260	1.64
2	0.282	0.391	1.38
3	0.282	0.391	1.38
4	0.282	0.391	1.38
5	0.280	0.387	1.38
6	0.279	0.383	1.37
7	0.222	0.332	1.47

Secondly, the domain height is increased to $H = 510\ \mu m$ as shown in Figure 5.5. Similar to the first case, as intra-tow porosity is kept constant at 50%, the inter-tow porosity increases to 33% and the overall porosity becomes 66%. The simulated and approximated overall permeabilities are provided in Table 5.4. As expected, overall permeability increases with larger domain height due to wider channel gaps between tows. In this scenario, the approximated and simulated overall permeabilities are closer, showing an agreement with a maximum ratio of 1.14.

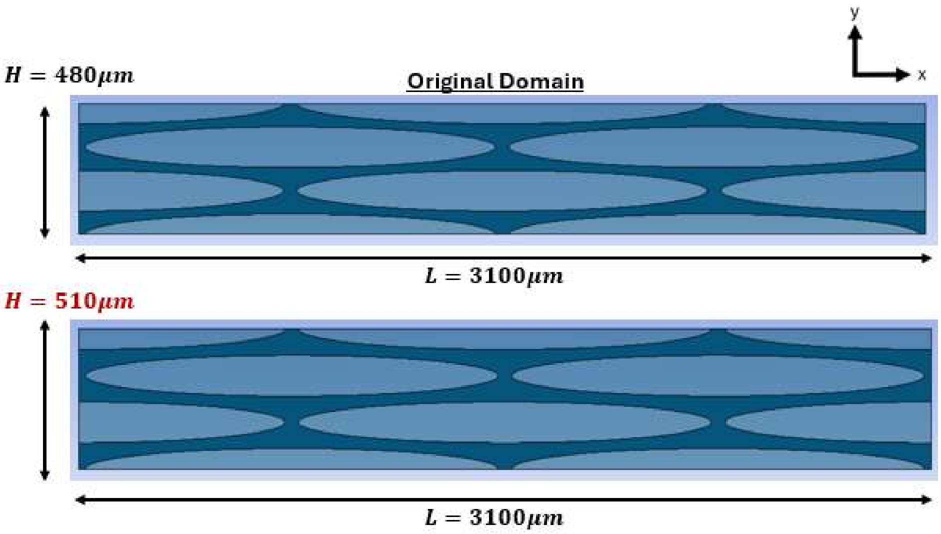

Figure 5.5: Tow domain for domain height $H = 510\ \mu m$

Table 5.4: Simulated and approximated permeabilities for domain height $H = 510\ \mu m$

Case	$K_{o,sim}\ [m^2]$ $(\times 10^{-10})$	$K_{o,app}\ [m^2]$ $(\times 10^{-10})$	$K_{o,app}/K_{o,sim}$
1	0.759	0.862	1.14
2	2.62	2.61	1.00
3	2.62	2.61	1.00
4	2.62	2.61	0.99
5	2.55	2.61	1.02
6	2.49	2.61	1.05
7	1.66	1.76	1.06

Ratios between the approximated and simulated overall permeabilities are compared for different domain heights as in Table 5.5.

Table 5.5: Comparison of approximated and simulated permeability ratios for different domain heights

Case	$K_{o,app}/K_{o,sim}$		
	$H = 450\mu m$ $\emptyset_t = 24\%$ $\emptyset_o = 62\%$	$H = 480\mu m$ $\emptyset_t = 29\%$ $\emptyset_o = 64\%$	$H = 510\mu m$ $\emptyset_t = 33\%$ $\emptyset_o = 66\%$
1	1.64	1.31	1.14
2	1.38	1.11	1.00
3	1.38	1.11	1.00
4	1.38	1.11	0.99
5	1.38	1.13	1.02
6	1.37	1.15	1.05
7	1.47	1.21	1.06

As expected, the ratio between approximated and simulated permeabilities decrease with increasing domain height. This trend is attributed to the dominance of resin flow in the inter-tow channels for wider domains. Even though the intra-tow porosity remains constant, less resin flows through the porous tows due to wider inter-tow channels. Therefore, the assumption of neglecting the resin flow in the porous tows in the permeability approximation becomes increasingly valid for larger domain heights.

Chapter 6:
CONCLUSION AND FUTURE STUDIES

This study investigates the permeability of unidirectional fiber tow distributions using ANSYS Fluent simulations based on Darcy's Law and compared the results with analytical solutions and permeability approximations derived from an electrical analogy. The computational modeling approach effectively predicted overall permeability, with representative unit cells of hexagonally distributed fibers matching Gebart's analytical formula results with a maximum error of 3.31%.

At a larger scale, the permeability of unidirectional fiber tow distributions is calculated by simulating resin flow in ANSYS Fluent and applying Darcy's Law. Key parameters such as tow spacing, domain size, and intra-tow porosity are systematically examined. Simulations revealed that varying tow distances, both manually and randomly, significantly influenced flow velocity distributions and channel formations. Wider inter-tow channels reduce flow resistance, increasing overall permeability, while narrower channels restrict resin flow. A correlation between overall permeability and channel gap is observed for gradually varying channel gap, demonstrating the importance of dominant flow channels in channel gap calculations. However, for random tow distributions within a fixed domain, no direct correlation is found between permeability and the channel gap parameters due to the limited sample size of 100 cases. This highlights the need for larger datasets to establish robust correlations.

The electric-hydraulic analogy-based permeability approximation demonstrates strong agreement with simulation results, achieving a maximum error of 31%. The approximation becomes more accurate as intra-tow porosity decreases and domain height increases, aligning with the assumption of negligible intra-tow flow.

This study confirms that the permeability approximation is a scalable and computationally efficient approach, reducing resources and time compared to full numerical simulations while maintaining reasonable accuracy. However, limitations in scenarios with high intra-tow porosity or reduced domain dimensions suggest areas for further refinement. Future research could focus on developing methods to incorporate intra-tow flow effects into the approximation model, which would improve its accuracy in cases where intra-tow porosity significantly impacts resin flow. Additionally, a larger sample size of random tow distribution variations could be analyzed to adopt a statistical approach, providing a more robust understanding of permeability behavior across different scenarios.

Further studies could also examine unit cells from both two-dimensional and three-dimensional domains to analyze the effects of warps and wefts in composite structures. This approach would allow for a more detailed investigation of intra-tow and inter-tow flows, offering deeper insights into the relationship between fabric architecture and resin flow dynamics. In addition, further studies could investigate permeability in other fiber architectures, such as biaxial, triaxial, or multi-layer woven fabrics, to expand the applicability of the models to a wider range of composite materials.

Overall, this work provides valuable insights into resin flow behavior and offers a practical framework for permeability prediction in fiber-reinforced composites.

BIBLIOGRAPHY

[1] S. G. Advani and E. M. Sozer, Process Modeling in Composites Manufacturing, Second Edition, New York: CRC Press, 2010.

[2] H. Darcy, Les Fontaines Publiques de la Ville de Dijon, Paris: Dalmont, 1856.

[3] R. Talreja, Failure Analysis of Composite Materials with Manufacturing Defects, CRC Press, 2024.

[4] D. Pantaloni, "A Review of Permeability and Flow Simulation for," *Materials,* vol. 13, no. 21, p. 4811, 2020.

[5] N. K. Naik, M. Sirisha and A. Inani, "Permeability characterizationofpolymermatrixcomposites," *ProgressinAerospaceSciences,* vol. 65, pp. 22-40, 2014.

[6] K. Nina, "Permeability characterization of dual scale fibrous porous media," *Composites: Part A,* vol. 37, no. 11, p. 2057–2068, 2006.

[7] H. Alotaibi, M. Jabbari and C. Soutis, "A Numerical Analysis of Resin Flow in Woven Fabrics: Effect of Local Tow Curvature on Dual-scale Permeability," *Materials,* vol. 14, no. 20, p. 405, 2021.

[8] M. Li, Y. Ren, D. Lee, M. Kim and S. Choi, "Effect of gelatin treatment on tow deformation in resin-impregnated glass fiber," *Scientific Reports,* vol. 12, 2022.

[9] B. R. Gebart, "Permeability of unidirectional reinforcements for RTM," *Journal of Composite Materials,* vol. 26, no. 8, pp. 1100-1133, 1993.

[10] A. Dei Sommi and F. Lionetto, "An Overview of the Measurement of Permeability of Composite Reinforcements," *Polymers,* vol. 15, no. 30, p. 728, 2023.

[11] R. Arbter, "Experimental determination of the permeability of textiles: A benchmark exercise," *Composites Part A: Applied Science and Manufacturing,* vol. 42, no. 9, pp. 1157-1168, 2011.

[12] N. Vernet, "Experimental determination of the permeability of engineering textiles: Benchmark II," *Composites Part A: Applied Science and Manufacturing,* vol. 61, pp. 172-184, 2014.

[13] R. S. Joemon, "Numerical investigation of VARTM process using finite volume method," *Materials Today: Proceedings,* vol. 11, p. 292, 2020.

[14] M. W. Tahir, "Effect of dual scale porosity on the overall permeability of fibrous structures," *Composites Science and Technology,* vol. 103, pp. 56-62, 2014.

[15] C. Zhao, "Three-Dimensional Numerical Simulation," *Applied Composite Materials,* 2019.

[16] H. Alotaibi, "A Numerical Thermo-Chemo-Flow Analysis of Thermoset Resin Impregnation in LCM Processes," *Polymers,,* vol. 15, no. 6, pp. 1572-1591, 2023.

[17] E. Syerko, "Benchmark exercise on image-based permeability determination of engineering textiles: Microscale predictions," *Composites Part A,* vol. 167, 2023.

[18] "ANSYS Fluent User's Guide," ANSYS, Inc., 2009.

[19] V. A. Kirsch, "Stokes Flow in Model Fibrous Filters," *Separation and Purification Technology,* vol. 58, no. 2, pp. 288-294, 2007.

[20] E. E. Swery, "Capturing the influence of geometric variations on permeability using a numerical permeability prediction tool," *Journal of Reinforced Plastics and Composites,* vol. 35, no. 24, pp. 1802-1813, 2016.

[21] A. Akers, M. Gassman and R. J. Smith, Hydraulic Power System Analysis, Florida: CRC/Taylo&Francis, 2006.

APPENDIX A: CASE STUDY FOR TWO POROUS REGION

A case study with a flow along a rectangular channel with two porous regions which have different porosities is solved analytically with the Darcy's Law, and numerically by using ANSYS Fluent. The result of the analytical solution and the experimental solution are compared.

The simulation is performed on a two-dimensional macro-scale flow domain. Figure A.1 shows the domain where two regions have different porosities and respectively different permeabilities. They are defined as porous zones with $K_{xx,1} = 2 \times 10^{-9}\ m^2$ and $K_{xx,2} = 8 \times 10^{-9}\ m^2$. No-slip boundary condition is assigned on the upper and lower boundaries which represents the channel. The inlet and outlet are defined as pressure inlet of $500\ kPa$ and pressure outlet of $100\ kPa$. The contact area between the first and second porous region is defined as an internal face boundary since there is a step change in the fluid characteristics.

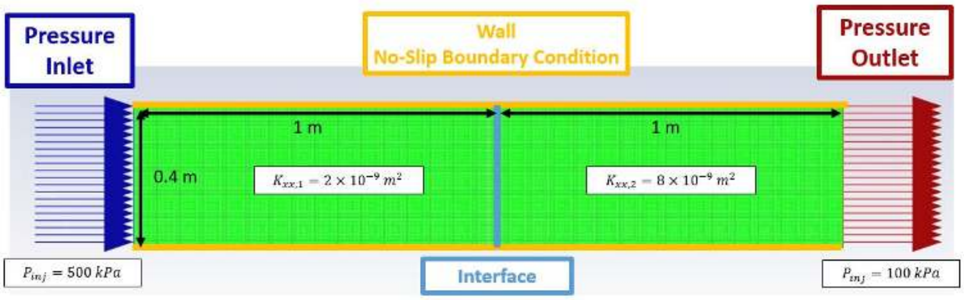

Figure A.1: Flow domain and boundary conditions for case study

The pressure value on the mid-point of the flow is equal to 180.001 kPa.

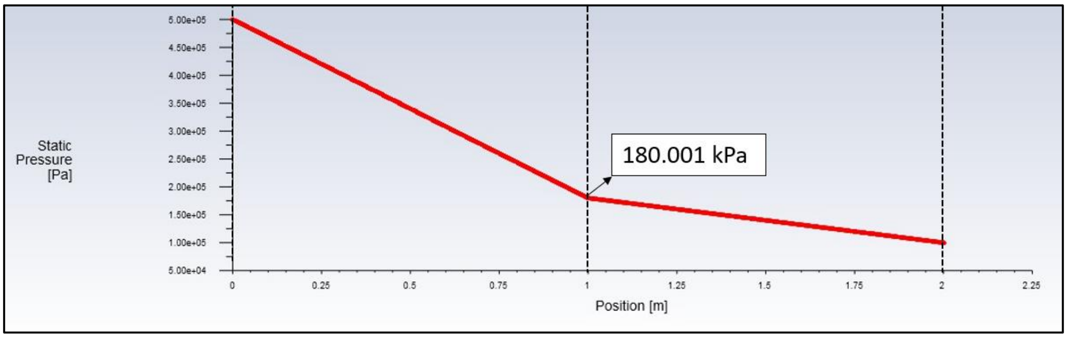

Figure A.2: Pressure graph from ANSYS Fluent for case study

For the analytical solution, flowrate must be constant for the conservation of mass.

$$u_1 A = u_2 A$$

$$u_1 = u_2$$

From Darcy's law, relation between pressures can be derived as below since the permeability and viscosity values are known.

$$-\frac{K_{xx,1}}{\mu}\left(\frac{\partial P}{\partial x}\right)_1 = -\frac{K_{xx,2}}{\mu}\left(\frac{\partial P}{\partial x}\right)_2$$

$$\frac{\left(\frac{\partial P}{\partial x}\right)_1}{\left(\frac{\partial P}{\partial x}\right)_2} = -\frac{\frac{P_{mid} - P_{in}}{x_{mid} - x_{in}}}{\frac{P_{exit} - P_{mid}}{x_{exit} - x_{mid}}} = \frac{K_{xx,2}}{K_{xx,1}} = \frac{8 \times 10^{-9}\, m^2}{2 \times 10^{-9}\, m^2} = 4$$

$$P_{mid} = \frac{P_{in} + 4P_{exit}}{5}$$

$$P_{mid} = \frac{(500\, kPa) + 4(100\, kPa)}{5} = 180\, kPa$$

The result from ANSYS simulation agrees with the analytical solution of the problem.

Table A.1: Pressure comparison for modelling and analytical solution of case study

	Analytical Solution	ANSYS Fluent Solution
Pressure (kPa)	180	180.001

APPENDIX B: CALCULATION OF PERMEABILITY FROM GEBART'S FORMULA

For the geometry in Figure 1.1, fiber volume fraction is calculated as below.

$$V_f = \frac{volume\ of\ fibers}{volume\ of\ mold\ cavity}$$

$$V_f = \frac{4\pi r^2}{ab} = \frac{4 \times \pi \times\ (2 \times 10^{-6})^2}{1.1547 \times 10^{-10}} = 44\%$$

From Gebart's formula, permeability perpendicular to the fibers is calculated as below.

$$K_{\perp\ hex} = \frac{16}{9\pi\sqrt{6}} \left(\sqrt{\frac{V_{f,max}}{V_f}} - 1 \right)^{5/2} r^2$$

$$K_{\perp\ hex} = \frac{16}{9\pi\sqrt{6}} \left(\sqrt{\frac{\frac{\pi}{2\sqrt{3}}}{0.44}} - 1 \right)^{5/2} (2 \times 10^{-6})^2 = 1.21 \times 10^{-13}\ m^2$$

APPENDIX C: CALCULATION OF PERMEABILITY FROM ANSYS SOLUTION

Figure C.1 shows the velocity vectors of inlet and outlet for the flow in x-direction for Unit Cell A in Chapter 2. For the permeability calculation, volumetric flow rate in the inlet is obtained from ANSYS Fluent.

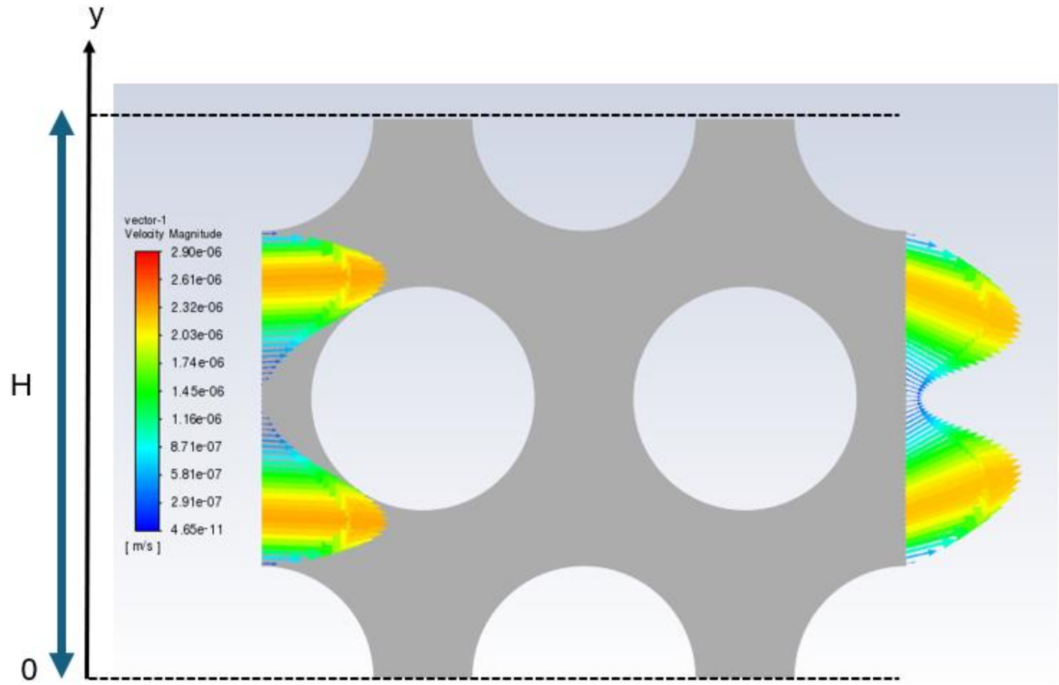

Figure C.1: Velocity vectors for flow through Unit Cell A

The flow is in x-direction, so we can write Darcy's Law in x-direction.

$$u_x = -\frac{K_x}{\mu}\frac{\partial P}{\partial x}$$

Volumetric flowrate is product of area and velocity.

$$Q_x = Au_x = -\frac{K_x A}{\mu}\frac{\partial P}{\partial x}$$

To find the volumetric flow rate along the input, we integrate it and obtain a relationship between volumetric flow rate and permeability.

$$Q_{inlet} = \int_0^H u_x Z dy$$

$$Q_{inlet} = -\frac{K_x H Z}{\mu}\frac{\partial P}{\partial x}$$

Volumetric flowrate is obtained from ANSYS Fluent as $7.15 \times 10^{-12}\,\frac{m^3}{s}$. Domain height is equal to $1 \times 10^{-7} m$. Domain thickness (Z) is taken as $1\,m$ for 2D simulations in ANSYS. Viscosity of the resin is $0.15\,Pa.s$. Pressure difference along the domain is $10\,kPa$, and domain lenght is $11.547 \times\ 10^{-6}\,m$.

$$Q_{inlet} = 7.15 \times 10^{-12}\,\frac{m^3}{s} = -\frac{K \times 1 \times 10^{-7} m \times 1m}{0.15\,Pa.s} \times \frac{10Pa}{11.547 \times\ 10^{-6}\,m}$$

$$K_x = 1.24 \times 10^{-13}\,m^2$$

Permeability in x-direction (K_x) is calculated as $1.24 \times 10^{-13}\,m^2$.

APPENDIX D: CALCULATION OF EFFECTIVE RESISTANCE

To be able to calculate effective resistance between points A and E, Delta to Star conversion is used shown in Figure D.1.

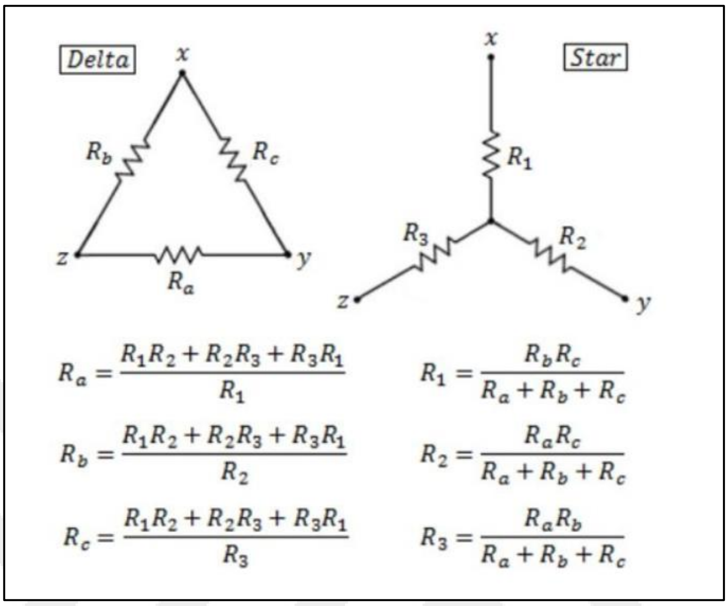

Figure D.1: Delta to star conversion

As a first step, delta #1 and #2 are converted to star formation as shown in Figure D.2. Resistances R_x, R_y R_z, R_k R_L R_m are defined as below.

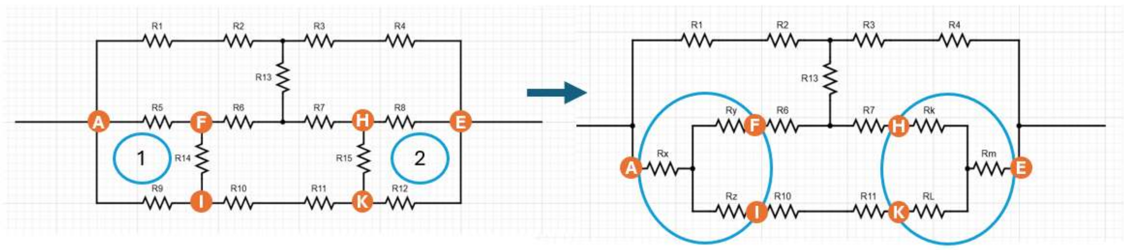

Figure D.2: Step 1 - conversion of delta #1 and #2 to star formation

$$R_x = \frac{R_5 \times R_9}{R_5 + R_9 + R_{14}}$$

$$R_y = \frac{R_5 \times R_{14}}{R_5 + R_9 + R_{14}}$$

$$R_z = \frac{R_{14} \times R_9}{R_5 + R_9 + R_{14}}$$

$$R_k = \frac{R_{15} \times R_8}{R_8 + R_{12} + R_{15}}$$

$$R_l = \frac{R_{15} \times R_{12}}{R_8 + R_{12} + R_{15}}$$

$$R_m = \frac{R_{12} \times R_8}{R_8 + R_{12} + R_{15}}$$

For the second step, delta #3 is converted to star formation as shown in Figure D.3. Resistances R_a, R_b R_c are defined as below.

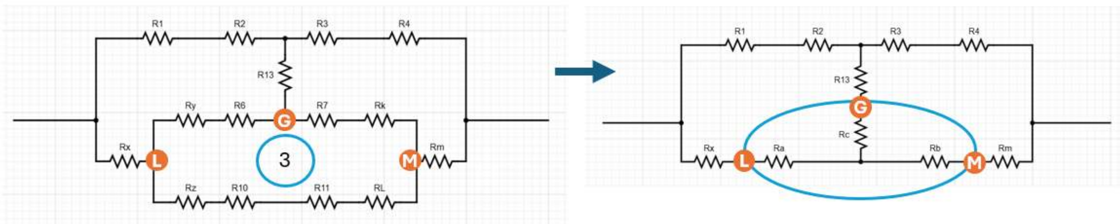

Figure D.3: Step 2 - conversion of delta #3 to star formation

$$R_a = \frac{(R_y + R_6) \times (R_z + R_{10} + R_{11} + R_L)}{(R_y + R_6) + (R_7 + R_k) + (R_z + R_{10} + R_{11} + R_L)}$$

$$R_b = \frac{(R_7 + R_k) \times (R_z + R_{10} + R_{11} + R_L)}{(R_y + R_6) + (R_7 + R_k) + (R_z + R_{10} + R_{11} + R_L)}$$

$$R_c = \frac{(R_y + R_6) \times (R_7 + R_k)}{(R_y + R_6) + (R_7 + R_k) + (R_z + R_{10} + R_{11} + R_L)}$$

For the third step, delta #4 is converted to star formation as shown in Figure D.4. Resistances R_i, R_j, R_p are defined as below.

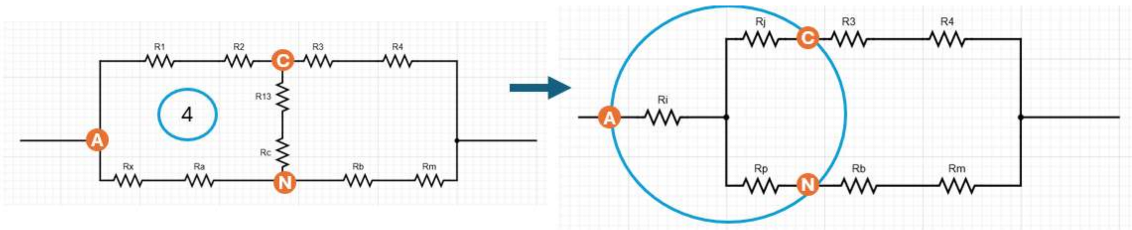

Figure D.4 Step 3 - conversion of delta #4 to star formation

$$Ri = \frac{(R_x + R_a) \times (R_1 + R_2)}{(R_x + R_a) + (R_1 + R_2) + (R_{13} + R_c)}$$

$$Rj = \frac{(R_{13} + R_c) \times (R_1 + R_2)}{(R_x + R_a) + (R_1 + R_2) + (R_{13} + R_c)}$$

$$Rp = \frac{(R_x + R_a) \times (R_{13} + R_c)}{(R_x + R_a) + (R_1 + R_2) + (R_{13} + R_c)}$$

Lastly, the effective resistance is written for resistors in the final formation shown in Figure D.5. R_{eff} is defined as below.

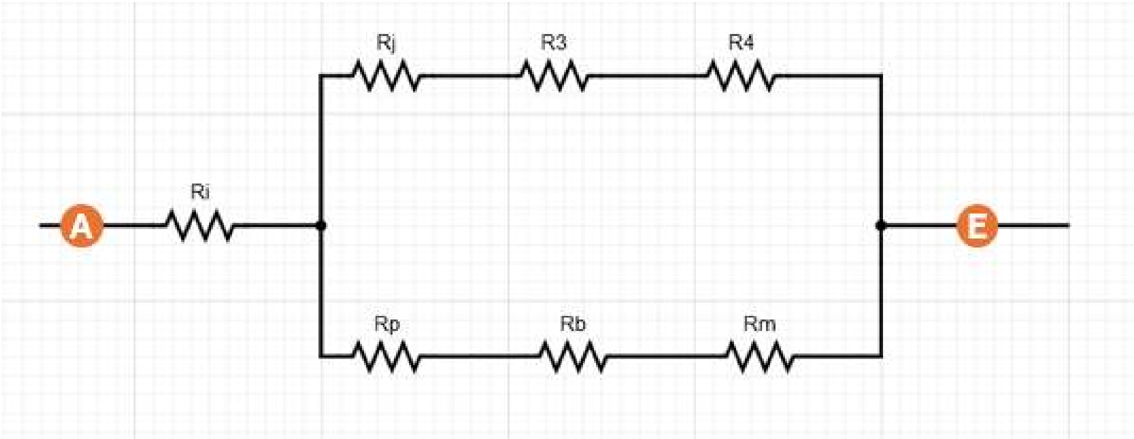

Figure D.5: Final circuit formation

$$R_{eff} = R_i + \left(\left(\frac{1}{R_j + R_3 + R_4}\right) + \left(\frac{1}{R_p + R_b + R_m}\right)\right)^{-1}$$